Geophysical Journal International

Geophys. J. Int. (2013) **192,** 113–136 doi: 10.1093/gji/ggs019

Erosion effects assessed by repeated gravity measurements in southern Taiwan

M. Mouyen,[1,2] F. Masson,[1] C. Hwang,[2] C.-C. Cheng,[2] N. Le Moigne,[3] C. W. Lee,[4] R. Kao[2,4,5] and W.-C. Hsieh[4,6]

[1]*Institut de Physique du Globe de Strasbourg, UMR* 7516*, CNRS et Université de Strasbourg (EOST), Strasbourg, France. E-mail: maximemouyen@gmail.com*
[2]*Department of Civil Engineering, National Chiao Tung University, Hsinchu, Taiwan* 300*, R.O.C.*
[3]*Géosciences Montpellier, UMR CNRS/UM2* 5243*, Université Montpellier* 2*, Montpellier, France*
[4]*Industrial Technology Research Institute, Hsinchu, Taiwan* 310*, R.O.C.*
[5]*Department of Geomatics Engineering, University of Calgary, Calgary, AB, Canada*
[6]*Graduate Institute of Geophysics, National Central University, Taoyuan, Taiwan* 320*, R.O.C.*

Accepted 2012 October 9. Received 2012 October 9; in original form 2012 May 07

SUMMARY

We analyse temporal variations of gravity measured in southern Taiwan since November 2006 at 10 sites using absolute gravimeters and, since November 2008, at 70 sites using a relative gravimeter. We describe and apply methods to interpret the gravity changes in terms of local hydrological processes and vertical ground motions. The effect of land water is computed from local rainfall data and a model of rain accumulation and discharge in the ground. The effect of the vertical motions of the ground is estimated using time-series of permanent Global Positioning System (GPS) stations and the theoretical gravity to height ratio of -2 μGal cm^{-1}. Unexpectedly, Morakot typhoon (2009 August), the strongest typhoon in Taiwan in 50 yr, was responsible for the highest gravity changes. Morakot triggered numerous large landslides and debris flow deposits. Their thicknesses are estimated from the gravity changes (up to ∼280 μGal) along with field observations and satellite images.

Key words: Time variable gravity; Hydrology; Creep and deformation; Asia.

1 INTRODUCTION

The study of temporal gravity changes enables to investigate processes that involve mass redistributions and vertical ground motions. This method is applied to several research areas such as volcanology (e.g. Furuya *et al.* 2003; Bonvalot *et al.* 2008), hydrology (e.g. Jacob *et al.* 2010) and tectonic deformation (e.g. Ballu *et al.* 2003; Mazzotti *et al.* 2007). The change of gravity combines all the processes due to mass transfers and deformation. Their respective parts must thus be identified prior to the analysis of one process in particular. The difficulty is that the part of each process can seldom be traced from gravity data only. Complementary observations and models are needed to identify them.

Numerous processes make the Earth gravity field vary with time. Reliable methods exist to take into account the effects of Earth tides (Dehant *et al.* 1999), ocean tide loading (e.g. Scherneck 1991; Matsumoto *et al.* 2001), polar motions and atmosphere (Torge 1989; Merriam 1992), which can thus be removed from the gravity time-series. An open issue is the contribution of hydrology, which influences gravity field both by deforming the Earth surface and by changing mass distributions at every spatial scale as well as at a wide range of temporal scales (minute to interannual). A hydro-gravity model, which focuses on gravity changes due to hydrology, requires parallel measurements of gravity and hydrological variables such as precipitation, soil moisture, water table depth (e.g. Lambert & Beaumont 1977; Bower & Courtier 1998; Kazama & Okubo 2009; Creutzfeldt *et al.* 2010; Pfeffer *et al.* 2010). Hydrology is a recurrent issue in the analysis of geodetic time-series because its effects are ubiquitous. If they are not removed, they could mislead the analysis of geodynamic processes (Dal Moro & Zadro 1998).

The Absolute Gravity in the Taiwan Orogen project (AGTO, Masson *et al.* 2008) was initiated in 2006 to study the geodynamics in Taiwan, which is located at the boundary between the Philippine Sea Plate and the Eurasian Plate (Fig. 1). Both plates converge at the rate of 8.2 cm a^{-1} (Yu *et al.* 1997) and Taiwan is the result of the collision of the Chinese continental margin (on the Eurasian Plate) and of the Luzon arc (on the Philippine Sea Plate). Two opposite subductions occur. In the north (Ryukyu trench), the Philippine Sea Plate is subducted below the Eurasian Plate, and inversely in the south (Manila trench). The deep processes involved in the mountain building are still to be clarified. One issue is to determine how the Chinese continental margin crust participates in the mountain building at depth and compensates for the exhumation and erosion of the Taiwan orogen. For instance it has been suggested that the

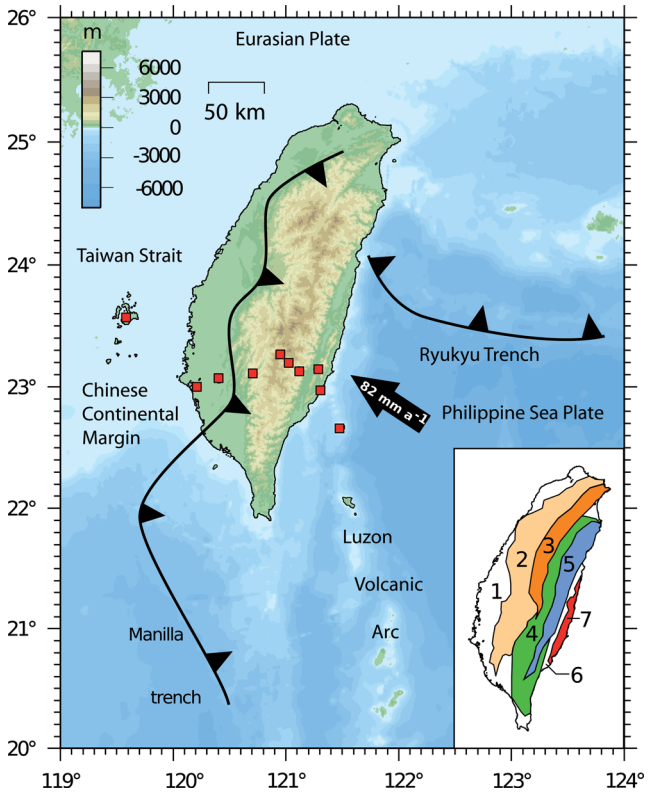

Figure 1. Tectonic context of Taiwan. A simplified map of the main tectono-physiographic ensembles is presented in the bottom right panel: 1, Coastal plain; 2, Western Foothills; 3, Hsuehshan Range; 4, Backbone Slates; 5, Tananao Complex; 6, Longitudinal Valley; 7, Coastal Range. The Longitudinal valley (unit 6) is considered to be the boundary between the Eurasian Plate (units 1–5) and the Philippine Sea Plate (unit 7). The Central Range is composed of units 3, 4 and 5. The red squares are the sites where absolute gravity (AG) is measured.

upper part of the Chinese continental margin crust is underplatted within the orogenic wedge, while its deeper part is subducted (Hwang & Wang 1993; Simoes *et al.* 2007). On the other hand, because of the likely buoyancy of the continental crust in comparison with Philippine Sea Plate, Yamato *et al.* (2009) proposed that the whole crust of the Chinese continental margin accretes into the orogen, without subducting. Presently, these different tectonic models explain the same data sets, based mainly on metamorphic and thermochronological observations. Additional data may help to better identify the orogeny processes (Simoes *et al.* 2012). Thus gravity measurements were carried out to bring new geophysical constraints to this debate. Meanwhile the gravity signal expected from the deep mass transfers is lower than 1 μGal a^{-1} (1 μGal = 1×10^{-8} m s^{-2}; Mouyen *et al.* 2009), which is a very small signal compared to the accuracy of absolute gravimeters (∼2 μGal). Besides, Taiwan experiences other processes related both to its tectonics and climate (vertical ground motions, hydrology, typhoons), which also contribute to gravity changes. Our aim is thus to investigate and separate the effects that have been recorded in the gravity time-series collected since 2006 in southern Taiwan.

In the paper, we first describe how the gravity data were acquired and processed. We then interpret the data, first by focusing on the effects of the vertical ground motions and hydrology in the gravity changes. We finally investigate the effects of landslides and debris flow deposits in our measurements.

2 DATA

2.1 Gravity network

Similar to GPS or levelling for ground displacements, the study of temporal gravity changes requires repeated gravity measurements. The observed gravity changes can only be explained by mass redistributions or ground deformations. 10 and 70 sites located across southern Taiwan were monitored by absolute and relative gravimetry, respectively (Figs 2a and b). The absolute gravity (AG) measurements started in 2006 November. They were performed once a year in November up to 2010. Practically, two Micro-g LaCoste FG5 absolute gravimeters were used in turn each year: FG5 #224 was operated by the Industrial Technology Research Institute (Taiwan) and FG5 #228 was operated by Géoscience Montpellier (France). The relative gravity (RG) surveys were also repeated in November using the same CG-5 Scintrex Autograv System, but were started in 2008. The AG measurements were performed on concrete pillars ($1 \times 1 \times 1$ m^3) buried with a few cm protruding from the ground. A benchmark indicates where to set the absolute gravimeter. The sites cross the main geological features of Taiwan, from the Philippine Sea Plate to the Eurasian Plate. The pillars were built nearby permanent GPS stations (Fig. 2a) so that vertical deformations can be studied along with gravity changes.

The RG network was set around the AG pillars in order to increase the spatial density of the gravimetric observations. The network contains the levelling benchmarks that exist along most of roads. We also added sites in the vicinity of permanent GPS stations. Note that there were slight variations in the visited points of the RG network for each survey.

1. *In 2008:* The survey spanned the south of Taiwan, from the Coastal Plain (West) to the Coastal Range (East). In total the survey visited 52 measurements sites: seven AG sites and 45 RG sites.
2. *In 2009:* We only repeated measurements on the eastern part of the 2008 network (east of AG05, Fig. 2b). Also, to the 26 existing points, 19 new sites (RG30–RG48, all are levelling benchmarks) were selected and measured in this area, where data are less noisy (possibly because of the lower amount of human activities and the more consolidated rocks). AG05, was swept away by typhoon Morakot in 2009 August, so totally, 44 sites were measured.
3. *In 2010:* The survey spanned the south of Taiwan, like in 2008, and integrated the 19 eastern sites added in 2009. It must be noted that five sites located west of AG05 were also destroyed by typhoon Morakot (RG03, RG09b, RG10, RG11 and SILNb) and that RG48 was not accessible in 2010. In total 64 sites were measured.

For data acquisition, both absolute and relative gravimeters must be levelled using tripods with footscrews to ensure that the sensors are aligned with the vertical component of the gravity. Indeed, gravimeter can only measure this component. The levelling may lead to instrumental heights variations between surveys, hence to gravity changes unrelated to geophysical processes. To avoid this confusion, the height of the FG5 sensor was systematically measured and taken into account during the data processing. For the CG-5, the tripod was customized by fixing one footscrew at a constant height. This fixed footscrew was always positioned exactly at the same place of the RG site, making the gravity sensor of the CG-5 be always at the same height for all repeated surveys.

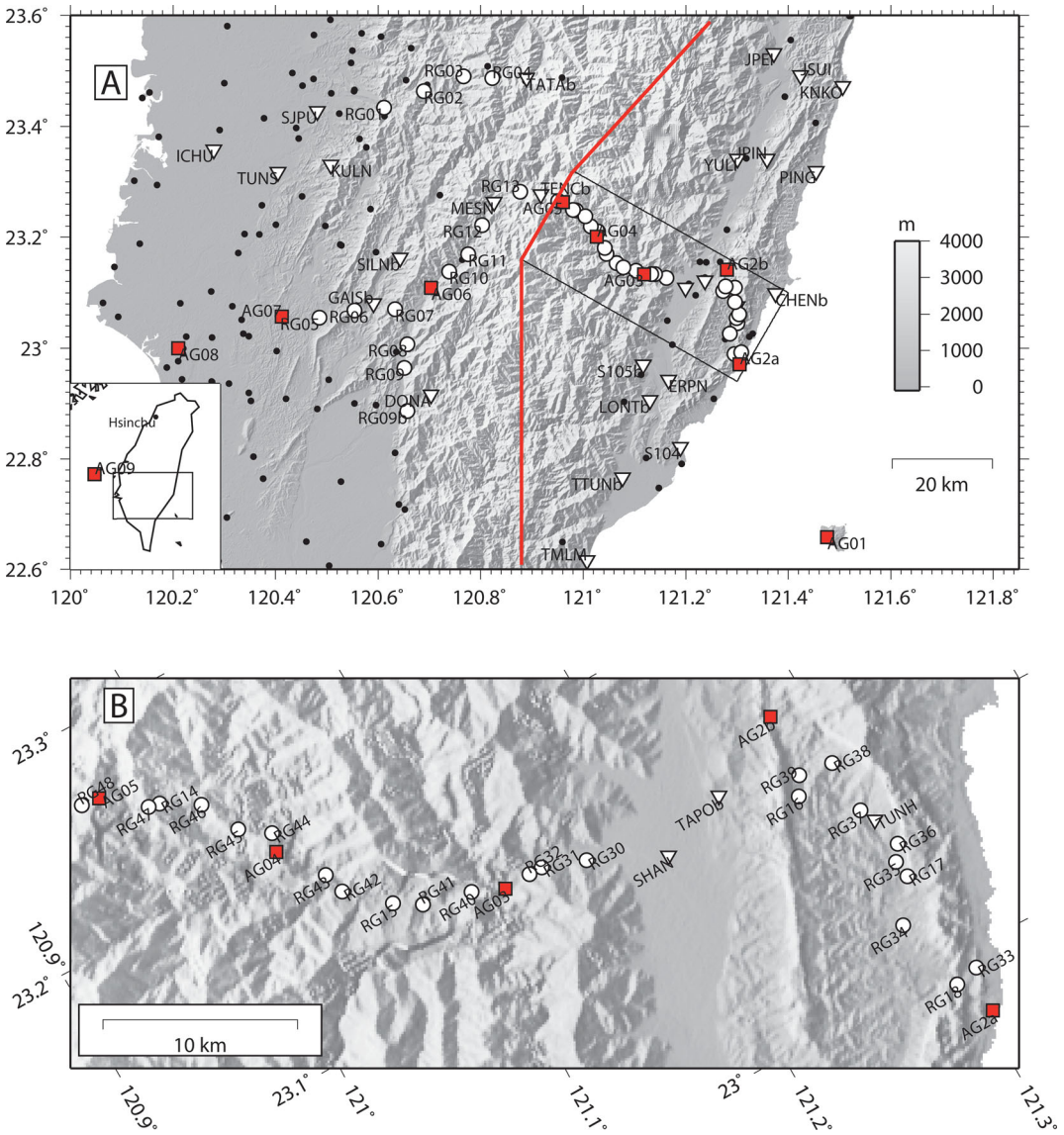

Figure 2. (a) Gravity measurements network: sites positions and names (the topography is shaded in the background). The general location of the network is displayed in the lower left map, also with AG09 position, on Penghu islands, and Hsinchu city. The red squares are concrete pillars built for AG measurements. The white circles and inverted triangles are levelling benchmarks and GPS stations, respectively, where relative gravimetry (RG) sites are performed. The smaller black dots are permanent GPS stations. Every site has a benchmark on the ground that allows to identically position the instrument from one survey to another. The RG sites measured in 2009 are located east of the red line. For more legibility, the names of the RG sites between AG05 and AG2a are given on map (b).

2.2 Instruments and acquisition

The FG5 absolute gravimeter measures the gravity value by the free fall of a test mass in a vacuum chamber. It contains a laser interferometer that measures the position of the test mass (a transparent corner cube) all along its free fall, and the time of each position by an atomic clock. The acceleration of the test mass, that is, gravity, can thus be determined. The superspring of the FG5 reduces the microseismic noise during measurements. Such seismic isolation is essential reaching ∼2 μGal of accuracy. A detailed description of these devices can be found in Niebauer *et al.* (1995) and in the FG5 documentation (Microg-LaCoste 2006). In this study, one AG measurement took about 12 hr. It was started in the evening when man-made noise and temperature variations were lower than day times. One set of 100 test mass drops started every 30 min (one drop every 10 s). About 24 sets were acquired and processed to determine the gravity value. The next site can be measured after 1 or 2 d, depending on the traveltime between each location. Two different FG5 were used in turn for each survey, the offset between both devices was determined in 2009 September during the 8th International Comparison of Absolute Gravimeters (ICAG) at the Bureau International des Poids et Mesures (BIPM, Paris, France). The gravity values from FG5 #228 were 2 μGal larger than those of the FG5 #224. This offset was added to the FG5 #224 values before constructing the gravity time-series.

The CG-5 measures gravity changes with space or time relative to a reference measurement. The sensor is a fused quartz spring and mass enclosed in a temperature stabilized vacuum chamber. A change of gravity implies a change of the mass that in turn changes the length of the spring. An electronic current immediately

Table 1. Loop organization of the relative gravity sites.

Loop	Sites included	Length (km)
1	AG07, ICHU, TUNS, KULN, SJPU, RG01	100
2	AG07, RG01, RG02, RG03, RG04, TATAb	130
3	AG06, RG07, GAISb, SILNb, RG06, RG05, AG07,	50
4	AG06, RG07, RG08, RG09, RG09b, DONA	40
5	AG06, RG10, RG11, RG12, MESN, RG13, TENCb, AG05	50
6	AG04, RG44, RG45, RG46, RG14, RG47, AG05, RG48	25
7	AG03, RG40, RG41, RG15, RG42, RG43, AG04	30
8	AG2b, TAPOb, SHAN, RG30, RG31, RG32, AG03	30
9	AG2a, RG33, RG18, RG34, RG17, RG35, RG36, TUNH, RG37, RG38, RG16, RG39, AG2b	40
10	AG2a, CHENb, PING, KNKO, JSUI, JPEI, YULI, JPIN, AG2b	135
11	AG03, ERPN, S105b, LONTb, TTUNb, TMLM, S104, AG2a	130

counteracts to maintain the spring at a constant length through a capacitive system. The injected current is measured and converted into a gravity value. This device allows to measure gravity changes with 5 μGal precision. Technical details are given in the user manual (Scintrex 2006). The CG-5 measurements are affected by instrumental drift, which must be corrected. One RG measurement took about 30 min. Gravity values were measured at a 6 Hz frequency and a mean value was stored every 90 s (Debeglia & Dupont 2002). In the fieldwork, we covered the gravimeter with a bottomless dustbin to avoid wind disturbances during the data acquisition. Also, we used an umbrella to protect the tripod from solar rays that warm it and rapidly alter the level of the device. At any site, the gravity acquisition was terminated as soon as the gravity variation in the three latest gravity readings (i.e. the three latest 90 sec means) was less than 5 μGal, and the readings did not show an increasing or decreasing trend. The internal temperature of the sensor chamber can change the spring properties, hence the gravity readings. To minimize this temperature effect, we used observations only after the internal temperature stability is reached (this parameter is displayed by the device along with the gravity readings). Typically, about 15 measurements were needed to fulfil these stability conditions and only the stable measurements (i.e. the last ones) were processed. On average, seven sites were measured per day. To estimate the gravimeter drift, the measurements are organized into loops (Table 1).

During the same day, we revisited several sites in a loop, and the first and last measurements were made at the same site. Each loop contained at least one AG site to constrain RG measurements. The relative gravimeter was also calibrated by computing the ratio of the gravity difference measured between two sites using both absolute and relative gravimeters (the AG difference is used as a reference) at locations with large gravity differences (>200 mGal), that is, sites with a high elevation difference, as recommended by Torge (1989). In addition, the CG-5 was used at each AG site to measure the vertical gravity gradient, which is needed when reducing the AG value at different heights (Section 2.4). The gradients were computed using RG measurements performed at three different heights (h_1 = ground level, h_2 = 60 cm and h_3 = 119 cm). The measurements at each height followed this order: h_1–h_2–h_3–h_2–h_1 and were made twice at each station.

2.3 Method to process the absolute and RG data

The AG values are processed with the g8 software, provided by Micro-g LaCoste (Microg-LaCoste 2008). The effects of solid Earth tides, ocean tide loading, polar motions and air pressure changes are removed from the 12 hr time-series at each site. Solid Earth tides are computed using ETGTAB (Wenzel 2002). Ocean tide loading effects are modelled from FES2004 (Letellier *et al.* 2004). Polar motion effects are computed using the formula from the Absolute Observations Data Processing Standards with the parameters from the International Earth Rotation Service and Reference Systems (IERS- http://hpiers.obspm.fr/). The air pressure correction is performed using a -0.3 μGal hPa^{-1} admittance factor (Torge 1989; Merriam 1992) and pressure data measured concurrently near the gravimeter.

The RG data are corrected for solid Earth tides using WDD theory (Dehant *et al.* 1999) and for ocean tide loading using TPXO 7.2 (Egbert & Erofeeva 2002), with the model parameters from the site http://froste.oso.chalmers.se/loading// provided by M.S. Bos and H.-G. Scherneck. The corrections are computed using TSOFT software (Van Camp & Vauterin 2005). Polar motion effects were neglected due to their small amplitude over the time of the survey ($\leq$1 μGal in 3 weeks), in comparison with the precision of RG data. The air pressure changes are corrected using data of the Central Weather Bureau (CWB) of Taiwan. The comparison of the CWB data with the air pressure measured during FG5 acquisition returns differences that account for 0.8 μGal at most. The CWB pressure data are thus reliable but an improvement would be to use a barometer concomitantly with the RG measurements. The gravimeter drift is then estimated using the MCGRAVI software (Beilin 2006), the principle is described in Hwang *et al.* (2002). A reliable way to test the quality of the drift adjustment is to measure each RG loop twice in a few days (in this study, 4 d, on average). Fig. 3 shows the difference of gravity obtained at each site of the RG network, between two measurements performed at time t and $t + 4$ d, for each of the three RG surveys. The gravity measurements reach 5 μGal repeatability at 89 per cent of the sites for the 2008s survey, 95 per cent for 2009 and 88 per cent for 2010. Thus most of the measurements match the precision of the gravimeter. This suggests that the tides, atmospheric and drift corrections, as well as the CG-5 calibration, are adequate.

2.4 Gravity changes since 2006 in southern Taiwan

The gravity changes measured by absolute gravimetry are displayed in Fig. 4. Gravity changes at time t are given in comparison with the value measured during the first gravity survey ($t_0 = 2006$), at every site. The uncertainty budget of the AG value is defined as

$$\delta_t = \sqrt{\frac{\delta^2}{N} + \delta_{\text{sys}}^2 + \delta_{\text{setup}}^2}, \quad (1)$$

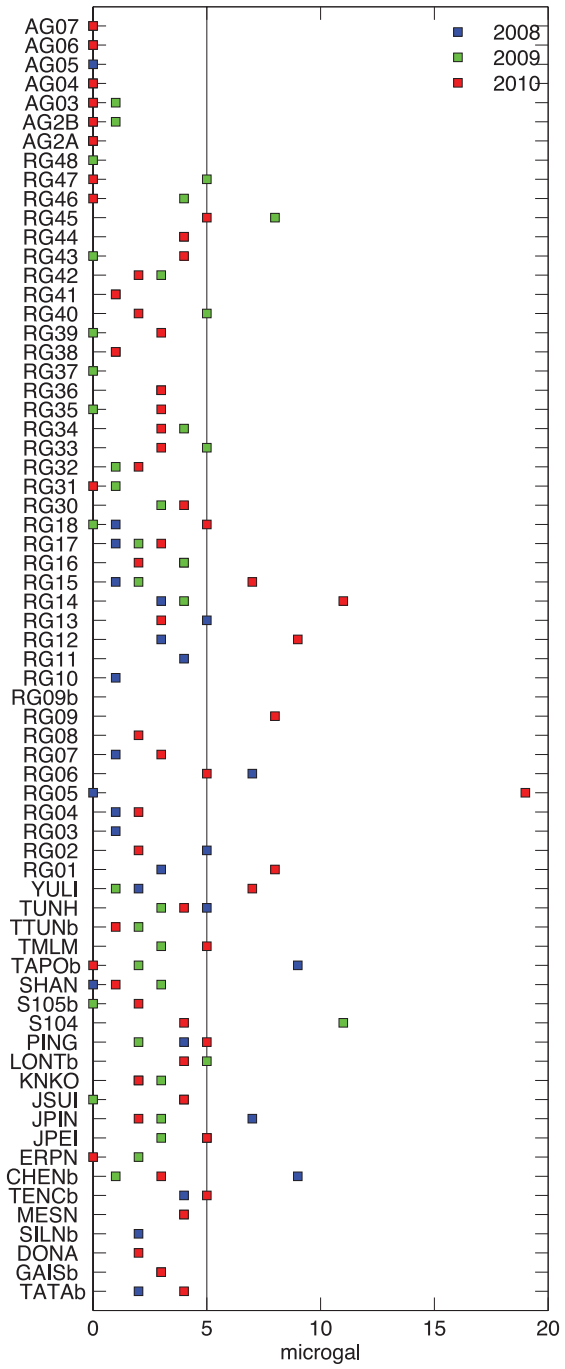

Figure 3. Repeatability of the RG results during each survey, in 2008, 2009 and 2010. The RG sites (excepted ICHU, TUNS, KULN and SJPU) were measured twice in 4 d. As no heavy rain or earthquake occurred during this time lapse, gravity value should be similar. The gravity change observed between two repeated measurements is lower or equal to 5 μGal at most of the sites.

where δ_t is the total uncertainty of the measurement for the survey at time t, δ is the standard deviation of the measurement (the set scatter), N is the number of sets for one measurement. δ_{sys} is the systematic uncertainty, inherent to the instrument and the applied corrections. It is estimated to be 1 μGal according to Niebauer *et al.* (1995). δ_{setup} is the instrument setup uncertainty, which is about 1.6 μGal (Van Camp *et al.* 2005). Another 1.6 μGal are also added when combining the results of the two different FG5 (Van Camp *et al.* 2005). Finally, the uncertainty of the AG change between the surveys at $t > 2006$ and the survey at $t_0 = 2006$ is

$$\delta_{t-2006} = \sqrt{\delta_t^2 + \delta_{2006}^2}. \quad (2)$$

The gravity changes measured by relative gravimetry are displayed in Fig. 5. The RG observations are constrained by AG values, which are reduced to the height of the relative gravimeter sensor using the vertical gravity gradients that were measured at each AG site. The same principle as in eq. (2) is applied, but using the initial measurement at $t_0 = 2008$ (2008 is the year of the first RG survey, see Section 2.1). Most significant gravity changes occurred in the Western Foothills, the Central Range and the Longitudinal Valley. Large gravity variations are found in these areas: they reach several tens of μGal at many sites (285 ± 3 μGal at RG12, 25 ± 3 μGal at AG06, −34 ± 4 μGal at RG02, between 2008 and 2010). In the Coastal plain, around ICHU, the large uncertainties (likely due to man-made noise) corrupt the gravity observations, despite the fact the gravity changes are larger than 10 μGal. By contrast, in the Coastal Range, the gravity changes are small (often lower than 5 μGal) and may be beyond the instrumental limit of the relative gravimeter.

3 EFFECTS OF LOCAL HYDROLOGY AND VERTICAL GROUND MOTIONS ON GRAVITY CHANGES

3.1 Modelling the effect of hydrology on gravity changes

The redistribution of water on land creates a Newtonian effect and a loading effect that combines ground vertical deformations and subsequent Earth masses redistributions. The temporal gravity changes caused by this process are observed at seasonal (Boy & Hinderer 2006; Longuevergne *et al.* 2009) and interannual timescales (Morishita & Heki 2008; Shum *et al.* 2011) as well as at the timescales of a few minutes, hours or days, in response to sudden heavy rainfall (e.g. Virtanen 2001; Meurers *et al.* 2007). In this study, gravity surveys were performed in the same month every year (November except in 2007 for AG03, AG04 and AG05, which were measured in 2008 March) to mitigate the seasonal influence of hydrology on the gravity changes. As the seasonal hydrological cycle is not perfectly periodic, and as water redistribution exits at several timescales, a remaining signal is identified in the gravity data.

We first study the influence of local water redistribution on gravity changes. Southern Taiwan climate exhibits summer wet/winter dry conditions (Chen & Chen 2003). The main rainy seasons are the early summer (mid-May to mid-June) and the late summer (mid-July to late August). On average, about three to four typhoons originating in the Pacific Ocean make landfalls on Taiwan from May to October. The peak of summer rainfall occurs in late July. The rains decrease from autumn (September to November) to winter (December to February), which is the driest season. Spring rains start again from late March, with a lower rate than in summer. Cheng *et al.* (2002) suggested that, in the forested area (covering AG2a to AG06), 52 per cent of the yearly precipitations turn into streamflows, which are formed by stormflows (direct flow) and baseflows in equal proportions. The stormflows are quickly evacuated to rivers, while the baseflows stay longer in the ground, thus participating in local water redistribution. The other 48 per cent are evapotranspirated by the vegetation. However we have no details about these processes, which are highly site-dependent. Therefore, to

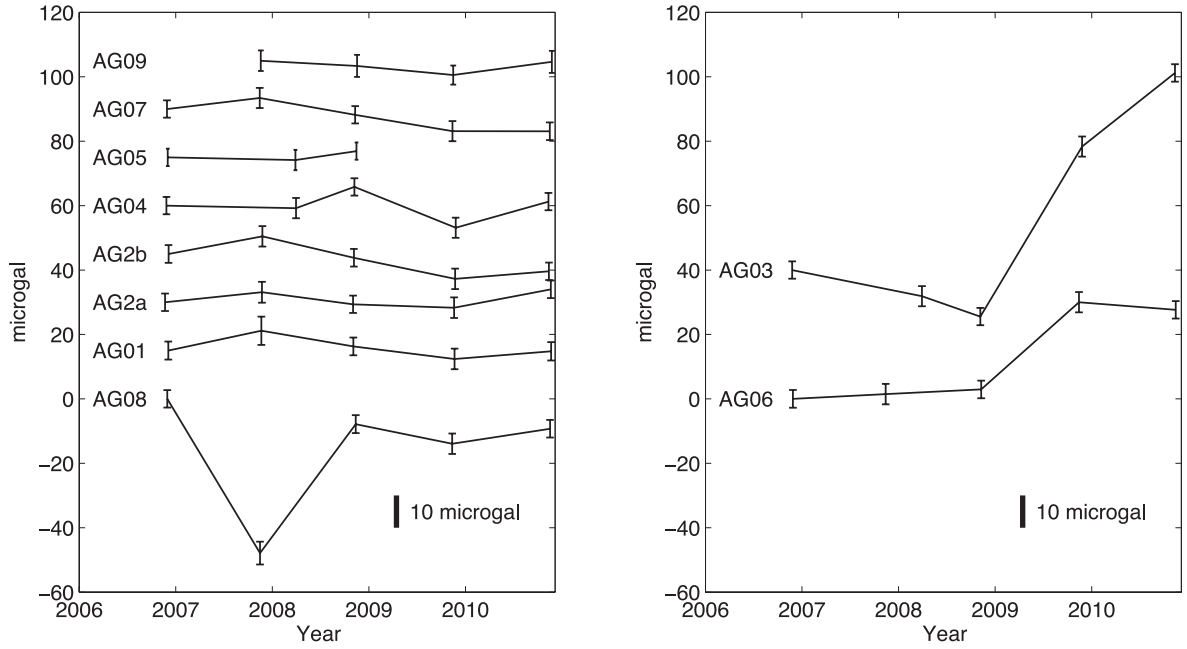

Figure 4. Gravity changes since 2006 measured by absolute gravimetry at the 10 AG sites located in Fig. 2. There are exceptions to the main protocol: (i) AG09 has been measured for the first time in 2007, (ii) in 2007, due to an instrumental problem with the FG5, sites AG03, AG04 and AG05 were not measured. A complementary survey was performed in 2008 March and (iii) AG05 was swept away by a landslide in 2009 August, terminating the gravity time-series in 2008 November.

investigate the effect of local water redistribution on the gravity change, we use the model proposed by Crossley *et al.* (1998), that allows to compute gravity changes from precipitation data collected nearby the gravimeter. The redistributed water is represented by an equivalent water table thickness, which accounts for the total mass of water that was redistributed, regardless of its reservoir (groundwater, soil moisture and vegetation). The amount of accumulated precipitation r_j at time j changes the equivalent water table thickness h_i at time i as

$$h_i = r_j[1 - \mathrm{e}^{-(i-j)/\tau_1}]\mathrm{e}^{-(i-j)/\tau_2}, \quad (3)$$

where τ_1 and τ_2 are time constants of the precipitated water charge and discharge below the gravimeter. The gravity effect can then be computed using the Bouguer Plate approximation

$$g_i = 2\pi g \rho h_i \quad (4)$$

where g_i is the gravity value at time i and ρ is the density contrast, that is, 1000 kg m^{-3}. The Bouguer Plate approximation implies that the water layer is modelled by a cylinder of thickness h_i, which radius x is infinite. At the μGal level, the 'infinite' cylinder can be regarded as a cylinder whose radius is larger than 400 m for a 1-m change of the water layer thickness, occurring at 10 m depth (and this radius decreases when the depth decreases): the difference between the effect of such a cylinder and an infinite cylinder is lower than 1 μGal. For water redistribution between 0 and 10 m depth, 99 per cent of the infinite cylinder effect occurs in a radius smaller than 1000 m. Therefore, this model only accounts for the effect of local hydrology, where the Newtonian attraction is responsible for most of the hydrological effects on gravity (e.g. Creutzfeldt *et al.* 2010).

We illustrate the quality of this model with continuous gravity data measured at the Hsinchu station, 200 km north of the gravity network (Fig. 2). The data were recorded with a superconducting gravimeter (SG) and are accessible through the Global Geodynamics Project database (GGP, Crossley *et al.* 1999). The SG raw data were corrected for solid Earth tides, ocean tide loading, polar motions, atmospheric pressure changes and instrumental drift (Hwang *et al.* 2009). Assuming that the gravity residuals (Fig. 6a, blue line) reflect land water changes near the gravimeter, we test the above local hydrological model with these residuals. The seasonal signal is not clearly observed in these data because the summer wet/winter dry conditions do not hold for northern Taiwan, where winter can be rainy too (Chen & Chen 2003). The topography around the SG station and the fact that it is underground might also contribute to lower the seasonal signal, as a consequence of the gravity compensation between water masses situated above and below the gravimeter. This was previously observed at Vienna (Van Camp *et al.* 2010), Membach (Meurers *et al.* 2007) and Moxa gravimetric observatories (Naujoks *et al.* 2008). The precipitation data measured near the SG station (Fig. 6b) are used in eqs 3 and 4. Parameters τ_1 and τ_2 are determined by forward modelling. τ_1 spans 0.1–20 d and τ_2 spans 2–100 d, with increments of 1 and 10 d, respectively. As the SG is underground (situated in a tunnel), water accumulates above the gravity sensor, that is, gravity decreases during rains. Possible pairs (τ_1; τ_2) are tested within these ranges by comparing the modelled hydrogravity time-series with the data (Fig. 6a, green line). The quality of the model is quantified by the rms misfit between the modelled and the observed gravity changes. Moreover, according to continuous gravity records at Hsinchu and at other locations in the world (Bower & Courtier 1998; Jacob *et al.* 2010), a realistic hydrogravity model should not result in gravity changes larger than 25 μGal (absolute value). The chosen pair (τ_1; τ_2) must thus return the lowest rms misfit among models, and the amplitude of gravity effect must be smaller than 25 μGal. We found $\tau_1 = 0.7$ d and $\tau_2 = 40$ d (rms = 3 μGal), with a nearly Gaussian distribution of the residuals around 0 μGal (Fig. 6c), suggesting that the method of Crossley *et al.* (1998) is appropriate for modelling the gravity effect of local land water, at least when gravity measurements are

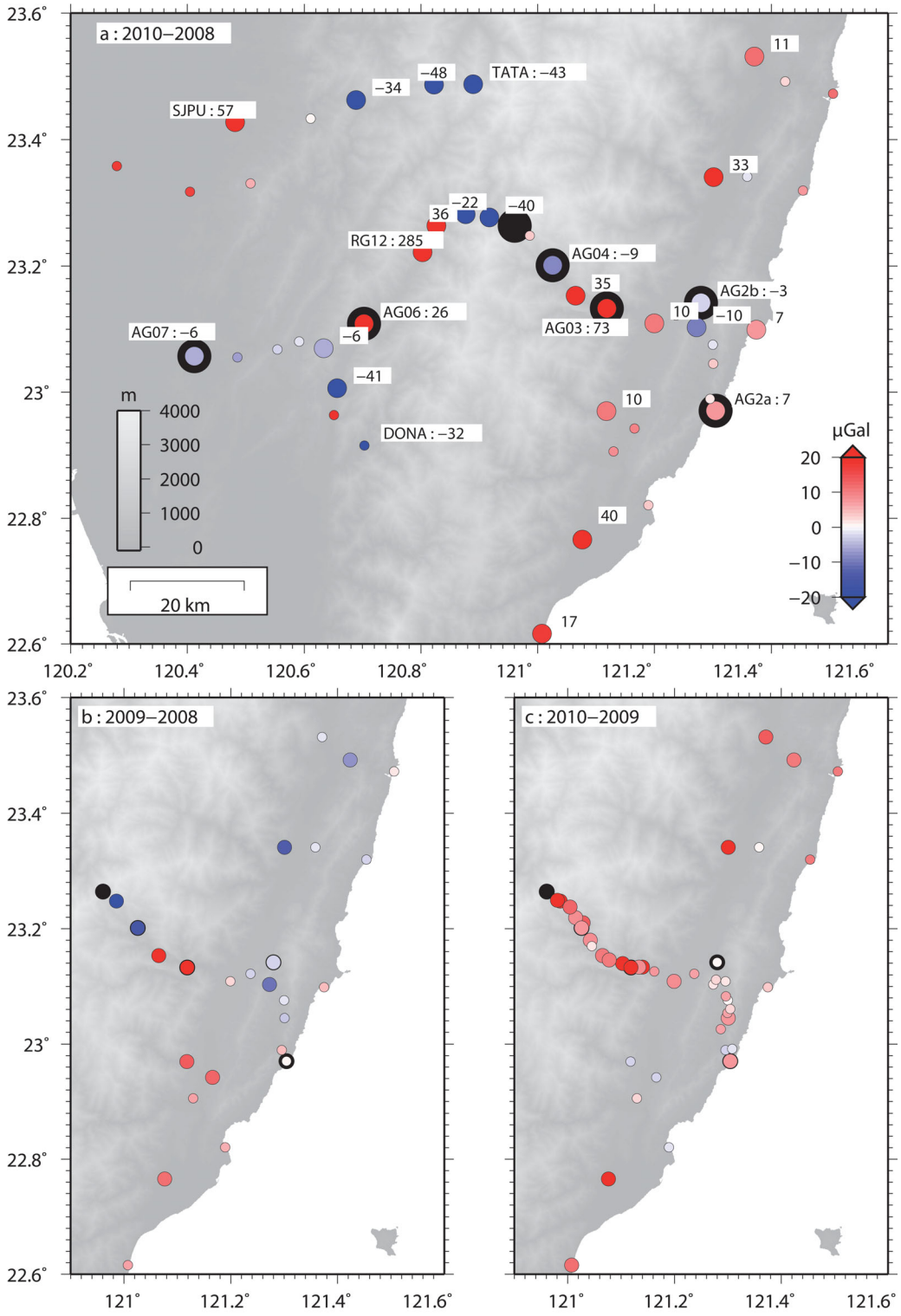

Figure 5. Results of the relative gravimetry surveys (the topography is shaded in the background). Significant gravity changes (larger than twice the measurement error) are displayed with a larger circle than not significant ones. AG sites are shown with a black circle in the background. (a) Gravity changes between 2008 and 2010. (b) Gravity changes between 2008 and 2009. (c) Gravity changes between 2009 and 2010. Six sites are missing in comparison with Fig. 2, swept away by landslides (like AG05) or debris flows: RG03, RG09b, RG10, RG11 and SILNb. Sites TENC and RG48 were not accessible in 2009 and 2010, respectively.

continuous. However, the gravity effect is systematically overestimated during heavy rain periods (Figs 6a and b). This is also visible in the larger amount of residuals between 5 and 10 μGal in Fig. 6(c). Probably, the model does not take into account a possible runoff of the rain when the ground is saturated: all the amount of rain is used to compute the gravity signal. We test this hypothesis by applying a weight coefficient (positive but smaller than 1) to heavy daily rains before the computation of accumulated precipitation. This

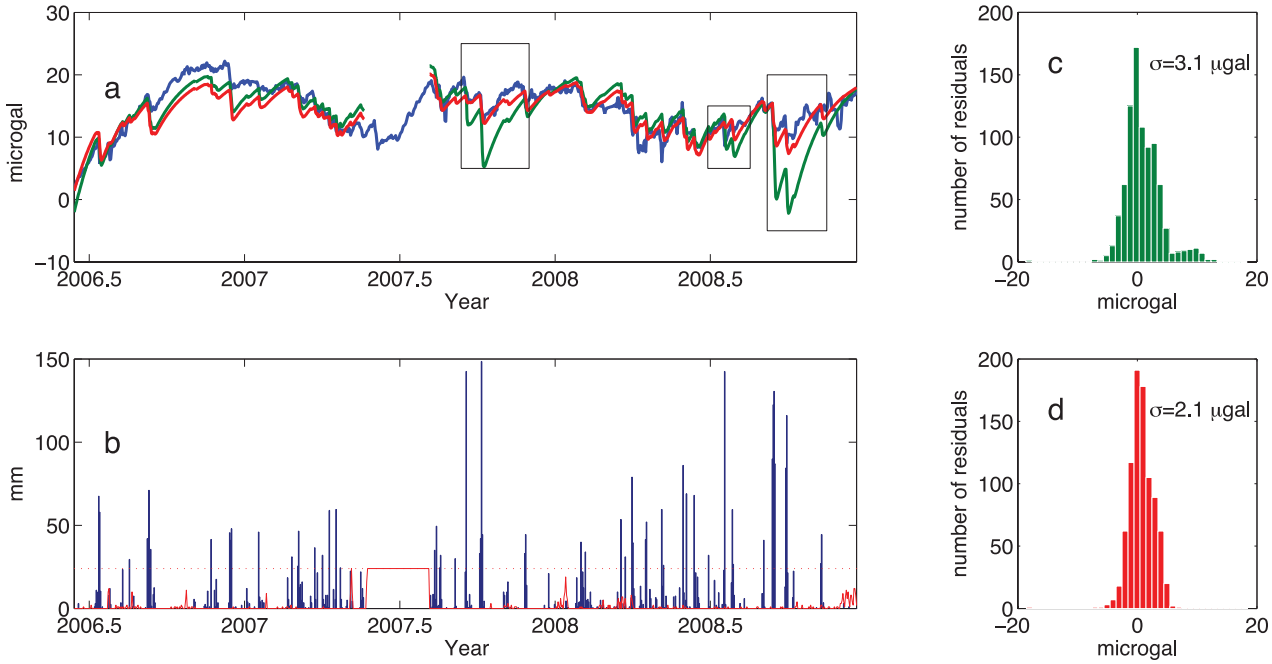

Figure 6. (a) Blue line: Residual gravity time-series of the superconducting gravimeter (SG) T048 at Hsinchu; this signal contains mainly changes due to land water redistribution. Green line: Gravity time-series modelled using eqs (3) and (4) and precipitation data recorded near the SG station. Red line: same as green but overestimations during large rains, underscored by boxes, has been reduced. (b) Blue bars: daily rains data (mm) used to model gravity changes. The red line is the number of missing hourly records per day (same axis as bars). Indeed we compute daily rains from hourly records. Thus it spans values between 0 and 24 (the limit at 24 is the short dashed red line). (c) and (d) are the histograms with standard deviations (σ) of the residuals obtained for the two models described above, without and with the correction of sudden large rains effects, respectively (same colour chart as a).

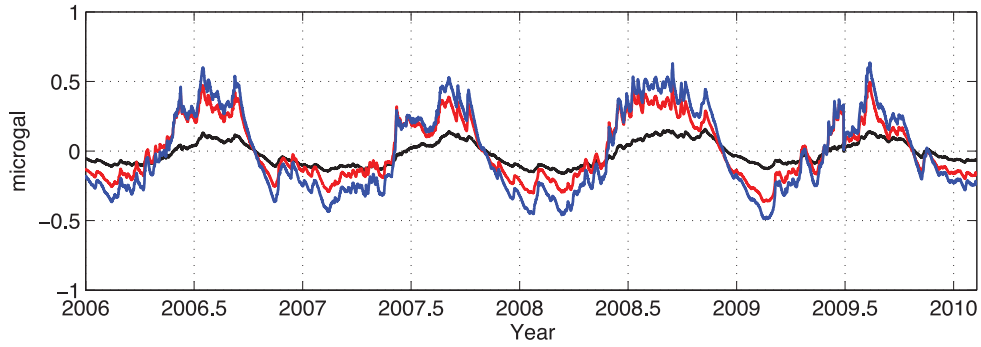

Figure 7. Gravity effect due to global water redistributions (blue line) computed at the SG location using the Global Land Data Assimilation System (GLDAS) hydrological model. It is the sum of the Newtonian effect (black line) and of the surface deformation plus Earth interior masses redistributions (red line).

modulation will only occur for daily rains above a threshold that we sought within a 50–200 mm range of daily precipitation. We finally reduce the rms discrepancies between the modelled and observed gravity changes from 3 to 2 μGal by considering that daily rains above 110 mm must only account for 10 per cent of the accumulated precipitation (Figs 6a, red line and d). A comprehensive investigation of this hypothesis is beyond the scope of this paper, and we never collected gravity data during such heavy rains.

We now focus on the effect of land water that is not distributed locally around the gravimeter. This gravity effect is modelled at Hsinchu (Fig. 7), again to allow the comparison with continuous gravity data. The modelling uses the Global Land Data Assimilation System (GLDAS, Rodell *et al.* 2004) and the Noah land surface model (e.g. Ek *et al.* 2003), which is available at a 3-hr temporal resolution and with a 0.25°-spatial resolution. Precipitations are forced by the Climate Prediction Center's Merged Analysis of Precipitation (ECMWF, Xie & Arkin 1997). Due to the spatial resolution of the Noah land surface model, the non-local (hereafter we write global) land water, is the land water everywhere except in a 0.25°-square area around the gravimeter. Fig. 7 shows that the global hydrological effects, which precision is about 1 μGal (Boy & Hinderer 2006), range from −0.5 to 0.5 μGal, and are even smaller during the gravity surveys. The prominence of the local hydrology effect and the sub-μGal amplitude of the global hydrology effect make the global hydrogravity model difficult to validate with the SG data. Moreover this signal is about 10 times smaller than the uncertainties of the gravity changes presented in Section 2.4. We therefore neglected it in our analysis.

3.2 Modelling the effect of vertical ground motions on gravity changes

Significant vertical ground motions exist in Taiwan (e.g. Huang *et al.* 2010; Ching *et al.* 2011; Peyret *et al.* 2011) and must be taken into account when interpreting temporal gravity changes. For

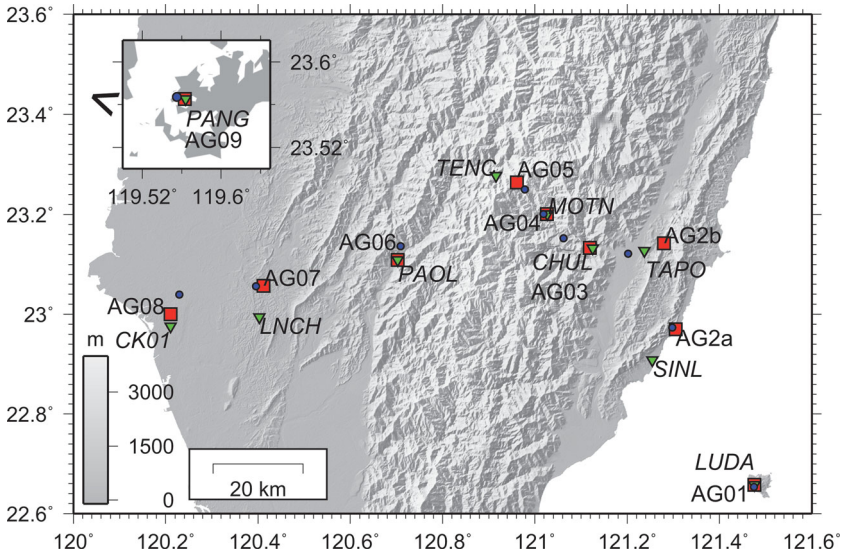

Figure 8. Locations of rain gauges (blue circle) and GPS stations (green inverted triangles, italic names. PANG station is located on Penghu island, west of Taiwan, Fig. 1) in comparison with AG sites (red squares). Each AG time-series is interpreted with the data from nearby GPS stations and rain gauges.

this effect, we adopt the complete Bouguer Plate reduction model (Hofmann-Wellenhof & Moritz 2006), with the theoretical ratio of $\Delta g/\Delta h = -1.967 \approx -2.0$ μGal cm^{-1}, where Δg is the change of gravity and Δh the change of height (positive upward). In fact, the $\Delta g/\Delta h$ ratio may vary with the process involved in the vertical deformation (e.g. de Linage *et al.* 2007). As an example for regions that experience glacial isostatic adjustment (GIA), Mazzotti *et al.* (2011) measured a $\Delta g/\Delta h$ ratio of -1.7 ± 0.1 μGal cm^{-1} in North America. This value is consistent with GIA model predictions and similar values (-1.6 to -2.0 μGal cm^{-1}) were also reported by Mäkinen *et al.* (2005) in the Fennoscandian GIA area. However in the case of Taiwan, the processes involved in vertical deformation have a tectonic rather than isostatic origin. They combine both the long-term mountain building and the shorter-term events of the seismic cycle and the determination of the $\Delta g/\Delta h$ ratio would need a complete modelling of these processes as well as experimental confirmations. Our gravity data are still too short for an experimental determination thus, according to Van Camp *et al.* (2011), we suggest that $\Delta g/\Delta h \approx -2.0$ μGal cm^{-1} is the most reasonable choice.

At every gravity site, the vertical ground motions can be estimated from the result of the Taiwanese permanent GPS network. Specifically, we used the vertical motions provided by the CWB (Shin *et al.* 2011) and processed using the Bernese software (Hugentobler *et al.* 2001). Daily solutions are computed in the ITRF2000 International Terrestrial Reference Frame (Altamimi *et al.* 2002) through the International GNSS Service (IGS) orbits. In the investigated areas the vertical velocities range from -1.53 ± 0.24 to 1.15 ± 0.06 cm a^{-1}, using Mazzotti *et al.* (2011) and Williams (2008) methods for analysing GPS time-series. The most significant subsidence rates are observed in the Coastal Plain (north of AG08, around ICHU, Figs 1 and 2) and in the western part of the Longitudinal Valley. The largest uplift rates are found in the Western Foothills, in the Coastal Range and in the eastern part of the Longitudinal Valley. Because the geographical pattern of the vertical motions is highly variable across Taiwan, we used GPS stations as close as possible to the gravity sites. Based on the tectonic maps of Shyu *et al.* (2005), there is no known active fault between the GPS and the gravity sites. Hence we can assume that the vertical movement measured by the GPS station are similar to those at the gravity site. The GPS-derived station heights were then averaged over the ± 10 d around the time of the gravity measurement. This averaged height is considered to be the station height at the time of the gravity measurement. The vertical motions are thus computed from the difference of these averaged heights. They represent the vertical deformations implied by both geodynamic processes and by seasonal loadings, especially those due to global land water redistribution, introduced in Section 3.1. Using the height changes and the ratio $\Delta g/\Delta h = -2.0$ μGal cm^{-1}, we estimate the gravity changes due to vertical ground motions.

3.3 Identification of tectonic and hydrological effects in the gravity data

The modelling methods presented in Sections 3.1 and 3.2 are first applied to the AG data. The AG data record is 2 yr longer than the RG record. The GPS stations and rain gauges used for the AG sites are shown in Fig. 8. We estimate the gravity effects of local hydrology by determining the values of τ_1 and τ_2 in two cases: one case with vertical ground motion corrected, and the other without such a correction. (Figs 9 and 10). The lowest rms misfits between the hydrogravity model and the gravity data in the two cases are summarized in Table 2. Our aim is to investigate whether the correction of the vertical ground motions improves the adjustment (lowers the rms misfit) between the hydrogravity model and the gravity data.

According to Table 2, the ground motion correction reduces the rms misfit at only 3 of the 10 AG sites: AG2b, AG07 and AG08. At the other sites, this correction does not improve the hydrogravity model, or even degrades it. However, we should only focus on the sites where this correction is significant in comparison with the uncertainty of the gravity measurements, that is, at AG2b, AG06 and AG07, where the rms misfits are changed by more than 1 μGal when the ground motion corrections are applied. Between the first (2006) and the last survey (2010), large uplift rates are observed at these sites: 1.15 ± 0.06 cm a^{-1} at AG2b, 1.01 ± 0.09 cm a^{-1} at AG06 and 1.10 ± 0.07 cm a^{-1} at AG07, which correspond to gravity decreases of 9.2 ± 0.5, 8.08 ± 0.7 and 8.8 ± 0.6 μGal, respectively, for the

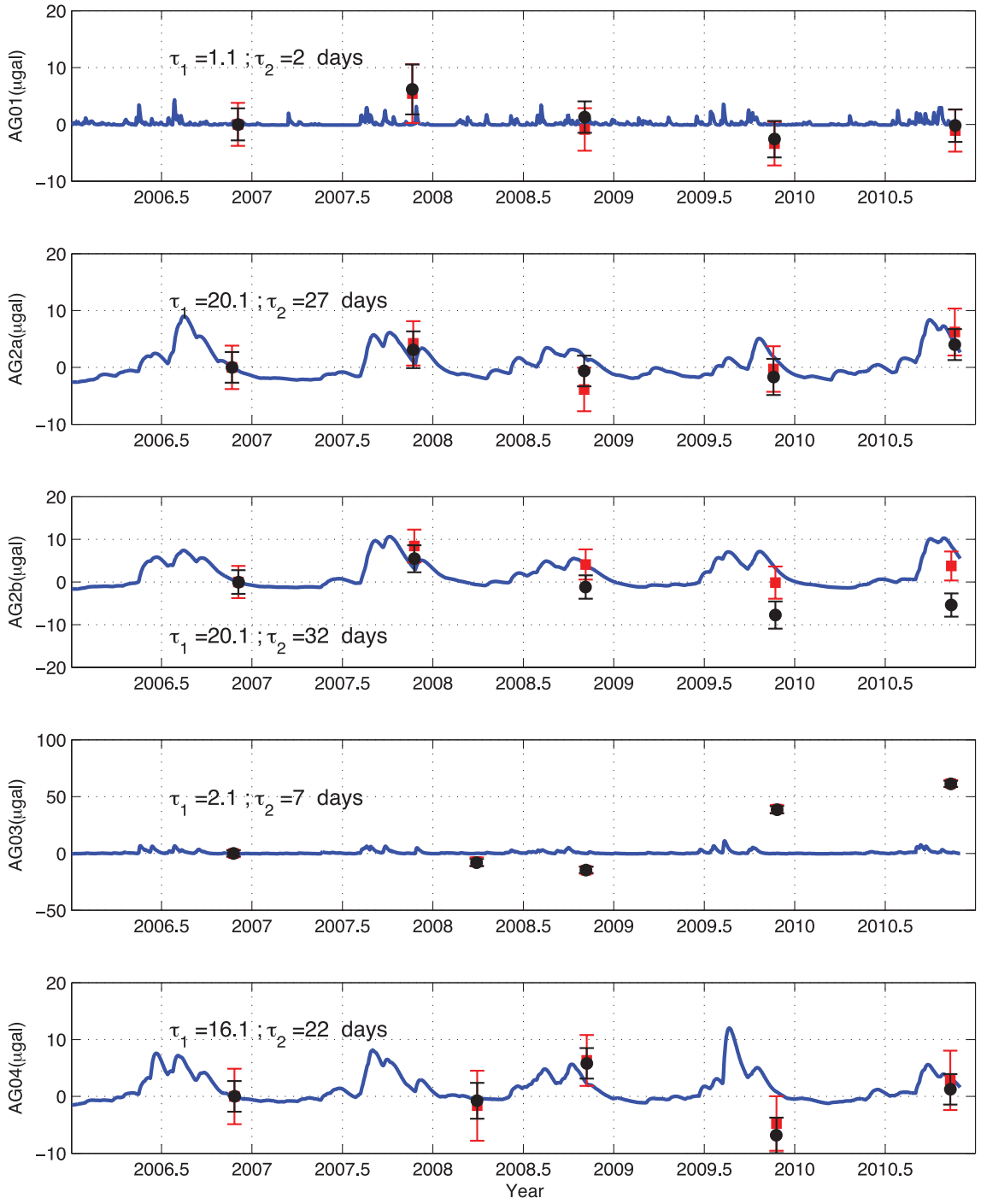

Figure 9. Hydrogravity model (blue line with τ_1 and τ_2 parameters, see Section 3.1) fit to the AG time-series corrected from vertical ground motions (red squares), concurrently measured by permanent GPS. We also show the fit of the hydrogravity model to gravity time-series not corrected from vertical movements (black dots). The latter hydrogravity model is not represented in these graphs but the rms misfit of each fit is given in Table 2. The GPS and precipitation time-series used at each AG site are provided in Appendix A.

entire length of the measurements (2006–2010). By correcting the vertical ground motions, the rms misfit between the AG data and the hydrogravity model is reduced by 1.6 μGal at AG2b and 2.3 μGal at AG07. However at AG06, the rms increased by 2.1 μGal, suggesting that the large uplift rate observed at this site is not properly taken into account. We give two reasons to explain this problem:

1. The gravity time-series shows a jump of 20 μGal after the third measurement, which will be explained by a debris flow deposit in the next section. Because of this jump we did not used the two last AG measurements in the adjustment of the hydrogravity model. Thus, the most significant part of the correction due to the uplift at this station is not taken into account and cannot help to reduce the rms misfit.

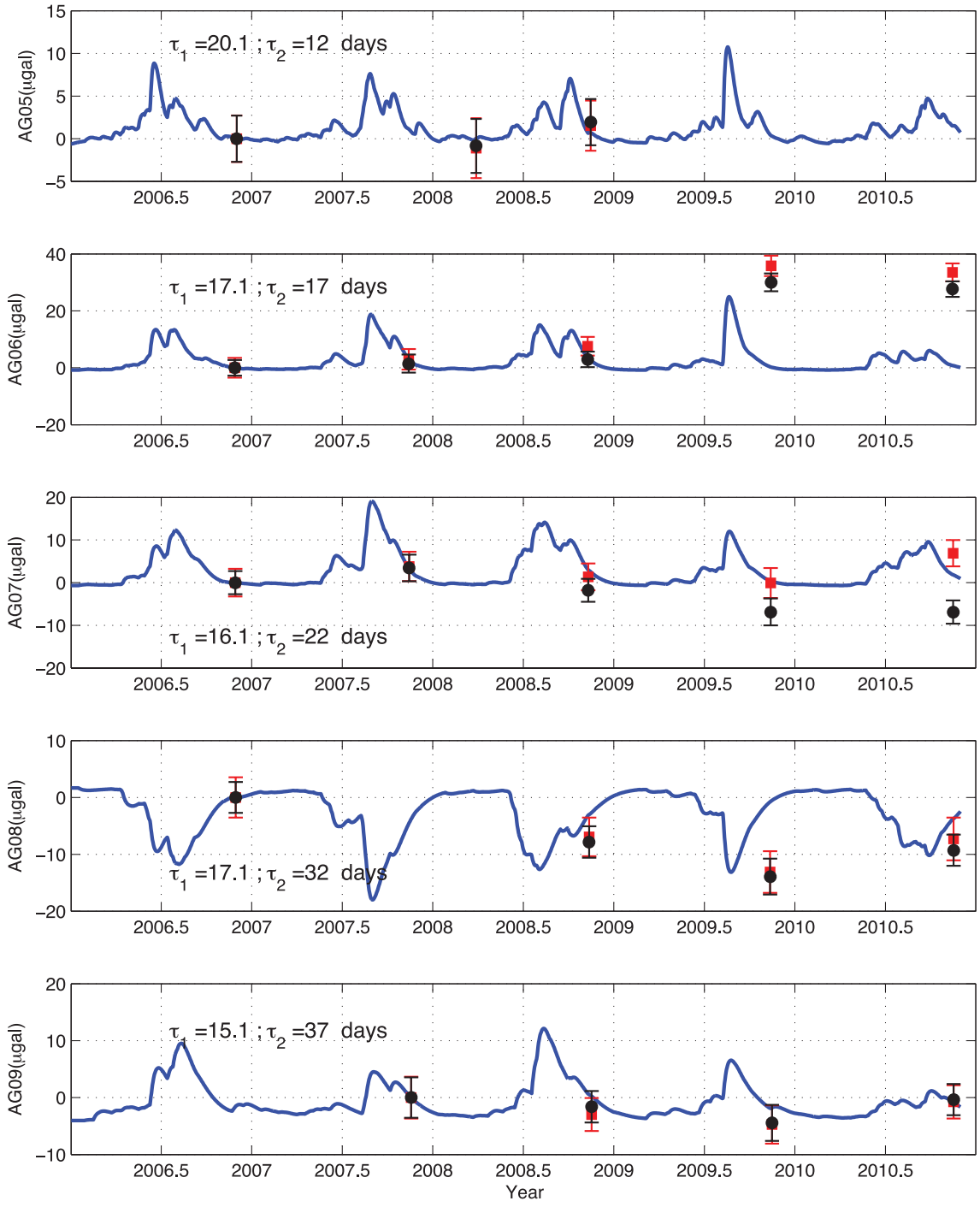

Figure 10. Same as Fig. 9 for sites AG05 to AG09. At AG06, only the three first gravity measurements are taken into account. The ∼25 μGal step after the third value (from 2008 to 2009) is discussed in Section 4.

2. This station is located only 300 m away from the large Kaoping river-bed, which meanders around it. Changes in the river level, and in turn the water mass, may introduce extra gravity effects in our model, which only considers land water redistribution.

Thus, considering our results at 2 of 3 AG sites where uplift rates are large, it is appropriate to remove the effects of vertical ground motions using $\Delta g/\Delta h = -2.0$ μGal cm^{-1}. Indeed, the AG data corrected for ground motion are better explained by local water redistribution. We cannot demonstrate the usefulness of this correction at AG sites where vertical motions are small (AG2a, AG04, AG05, AG08 and AG09). At these sites, the hydrogravity model computed from the precipitation data is suitable to understand gravity variations (except for the AG04 and AG08 measurements in November 2009 and 2007, respectively). The rms misfit shows little variations, hence little constraint, on τ_1 (Fig. 11), which is the charge time constant of the ground during rains. As there was no rain during gravity surveys, τ_1 could not be precisely determined. This could be improved by additional gravity measurement during heavy rains, for example, in July or August, according to the

Table 2. Rms misfits obtained between a hydrogravity model, that is, a pair (τ_1; τ_2), and gravity changes corrected (g_{corr}) or not ($g_{not\ corr}$) from vertical ground motions. The third column is the change of rms when vertical ground motions are corrected.

Site	A = rms misfit with g_{corr} (μGal)	B = rms misfit with $g_{not\ corr}$ (μGal)	Change of rms misfit (A–B) (μGal)
AG01	3.0	3.0	0.0
AG2a	2.4	2.1	0.3
AG2b	3.3	4.9	−1.6
AG03	9.6	9.6	0.0
AG04	1.6	1.5	0.1
AG05	0.5	0.5	0.0
AG06	2.6	0.5	2.1
AG07	2.4	4.7	−2.3
AG08	6.8	7.5	−0.7
AG09	2.4	1.6	0.8

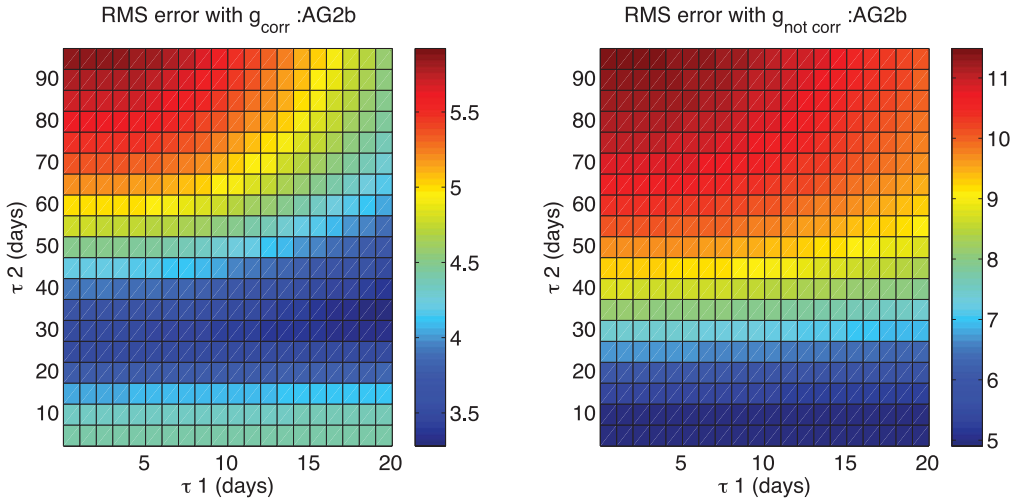

Figure 11. Example of the change of the rms misfit between the hydrogravity model and the gravity time-series at this site at AG2B. The fit is performed both using gravity time-series corrected (g_{corr}) and not corrected ($g_{notcorr}$) from vertical ground motions. They give the best pairs (τ_1; τ_2) that can be found in each case (i.e. with lower rms values). Note the lower range of the rms colourbar with g_{corr}. Little variation along the τ_1-axis is observed at AG2B, as well as at every site.

precipitation characteristics in southern Taiwan. To test how the use of only one gravity measurement per year affects the hydrogravity model definition, we applied it to the SG data again, but only using one gravity value per year (in total three values), instead of the entire time-series. Ten sets of gravity values are used, and they correspond to the same times as those at which the 10 AG sites have been measured (Fig. 12). The variance of the residual time-series is reduced from 15 to 9 μGal, when the hydrogravity model is removed. The 10 attempts yield average values of $\tau_1 = 13 \pm 4$ d and $\tau_2 = 36 \pm 3$ d. In Section 3.1, using the entire SG time-series, we found $\tau_1 = 0.7$ d and $\tau_2 = 40$ d. The τ_2 value is similar for both determinations. Indeed, as gravity values are taken at the end of the rainy seasons, they are more relevant to constrain the discharge of water. On the other hand, τ_1 is about 18 times higher than the best value found with continuous data. This confirms (along with Fig. 11) the weak reliability of τ_1 when it is constrained by gravity values sampled at a low frequency, in particular during dry epochs. Therefore, despite temporal gravity changes corrected from vertical ground motions are likely due to water redistribution, the hydrogravity model we use remains to be tested with gravity data sampled more frequently.

We also applied vertical ground motions corrections and hydrogravity adjustment to the RG measurements. The RG time-series, starting in 2008, are shorter than the AG ones, and some sites even contain only one gravity difference. However, if we consider that a rms misfit lower than 5 μGal is satisfactory, our interpretation method could explain the gravity changes at 20 of 25 sites over the Longitudinal Valley and the Coastal Range. Also, the correction of the vertical ground motions reduces the rms misfit at 70 per cent of these sites (Appendix B).

In summary, gravity changes from both AG and RG can be explained by combining:

1. GPS measurements and the theoretical ratio $\Delta g/\Delta h = -2.0$ μGal cm^{-1}, to account for vertical ground motion effects and
2. precipitations data acquired in the vicinity of the site where gravity is measured, to account for local hydrology effect. However, the lack of measurements during rains prevents from determining τ_1 unequivocally. This may return a biased hydrogravity time-series. Nevertheless, local hydrology has still to be considered as an efficient source of gravity changes.

It must be noted that, once the gravity time-series are corrected for vertical ground motions, the entire remaining signal will be used to constrain the hydrogravity model. There are two possible cases. The first case is that the hydrogravity model fits the corrected gravity data at the level of their uncertainties, and the residuals are not significant anymore for identifying a third signal. The second case is that no hydrogravity model can be properly constrained. In the latter case, one or several effects not related to local hydrology still exist in the gravity data and bias the estimation of the hydrogravity model. In our case we cannot fully explain the large gravity changes

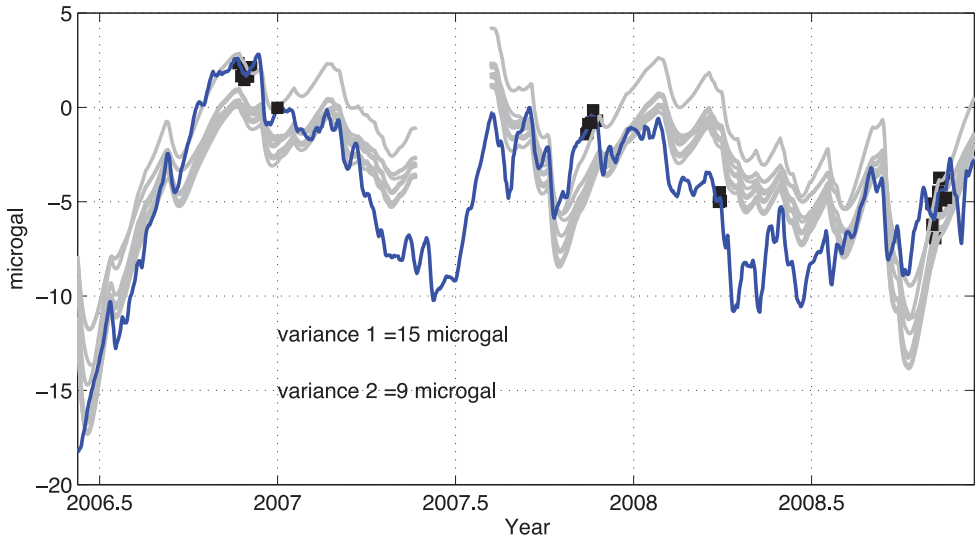

Figure 12. Grey lines: Gravity time-series modelled using eqs (3) and (4) and precipitation data recorded near the SG station. In comparison with Fig. 6(a), only 3 SG residual measurements are used (one per year, black squares) instead of the entire residual time-series (blue line). By residual gravity time-series we mean gravity time-series corrected from tides, polar motions, drift and atmospheric pressure. We test totally 10 sets of three measurements, which time correspond to those of the 10 AG measurements. The hydrogravity model reduces the variance of the SG time-series from 15 μGal (variance 1) for the original data (blue line) to 9 μGal on average (variance 2), when the hydrogravity model is subtracted.

at AG03 and AG06, located in the Central Range and the Western Foothills, respectively, and at more than half of the RG sites which are also located in these regions. A possible reason is that the rain gauges are not rigorously collocated with the gravity sites (Fig. 8). The large spatial variability of the rainfall in Taiwan, partly due to the mountain range (Chen & Chen 2003), could thus bias the hydrogravity model. However, the misfits reach several tens of microgals, which are difficult to model by only considering local water redistribution. As given in Section 4, these changes will be investigated in connection to the active erosion processes in Taiwan (Hovius *et al.* 2000; Dadson *et al.* 2003; Tsai *et al.* 2010). The role of shallow mass transfers implied by landslides and debris flows in such large gravity changes will be identified.

3.4 Effect of the aquifers

Despite encouraging results at many gravity sites, the estimation of hydrological gravity changes from rainfall data failed at SJPU, KULN, TUNS, ICHU and AG08 over the Coastal Plain. In fact, the failures occur for sure only at SJPU and AG08, because the uncertainties of gravity changes at KULN, TUNS and ICHU are much larger than the gravity changes. Nevertheless, the use of rainfall data only in this area must be discussed because these sites are located above aquifers used for water supply (Hsu 1998). The change in groundwater level is therefore also affected by artificial pumping that we did not take into account. In addition, the southern Coastal Plain experienced large flooding during typhoon Morakot (Ge *et al.* 2010). Flooding results from runoff of rain over large areas and therefore cannot be quantified by local rainfall data. The gravity change measured at SJPU (57 ± 10 μGal between 2008 and 2010) is equivalent to a 1.3-m-thick infinite layer of water. A further analysis of groundwater levels around SJPU will help to verify this hypothesis. It is also worth noting that the second measurement at AG08 (2007 November) is out of range in comparison with other values (Fig. 4). A problem of the atomic clock used with FG5#224 is suspected. Also, as AG08 is located in a building basement, this gravity change might be man-made. We eventually choose to not interpret this offset.

4 EFFECTS OF EROSION AND SEDIMENTATION PROCESSES IN GRAVITY CHANGES

4.1 Evidences of the signature of landslides and debris flow deposits in gravity changes

In early 2009 August, Taiwan was struck by typhoon Morakot, which brought the heaviest rains in 50 yr (Ge *et al.* 2010). Morakot triggered numerous landslides (Tsai *et al.* 2010), which then created large deposits (landslide-triggered debris flow deposits) in the riverbeds that cross the southern Central Range and Western Foothills. During the gravity surveys in 2009 November and 2010 November (after Morakot), we noticed substantial changes of the land morphology nearby several AG and RG sites (Table 3, and Fig. 13). Table 3 shows large gravity changes over the areas with large deposits or landslides, making it possible to associate gravity change with typhoon-induced surface process. Neither vertical ground motion nor local hydrology can explain these large gravity jumps. Fig. 14 shows the link between these large gravity changes and the topography, the latter partly controlling the landslides and deposits locations. The gravity changes observed in the Central Range and in the Western Foothills from 2008 to 2010 were compared with

Table 3. Gravity changes and landslides or debris flow deposits, observed in the Central Range and in the Western Foothills.

Site	Surveys	Gravity changes (μGal)	Morphological change
RG08	2008–2010	-41 ± 11	Landslide and deposit
RG09	2008–2010	18 ± 12	Deposit
DONA	2008–2010	-32 ± 19	Landslide
AG06	2008–2009	27 ± 2	Deposit
RG12	2008–2010	285 ± 3	Deposit
AG03	2008–2009	49 ± 1	Deposit

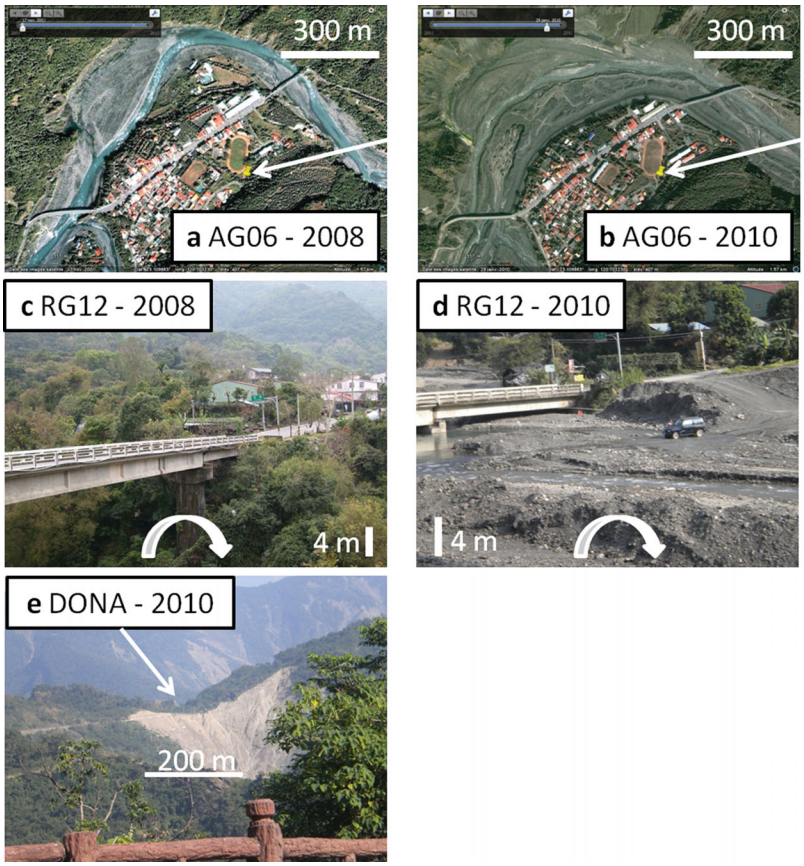

Figure 13. Pictures from Google-Earth (a and b) and from fieldwork (c–e), showing examples of debris flow deposits at AG06 (a and b, the deposit is in the river-bed) and at RG12 (c and d, the deposit is below the bridge) and of landslide at DONA (e, foreground light brown space in the forest). Except for DONA, we show pictures before and after Morakot typhoon to underscore its consequences on the land morphology. The white arrow locates the gravity site position.

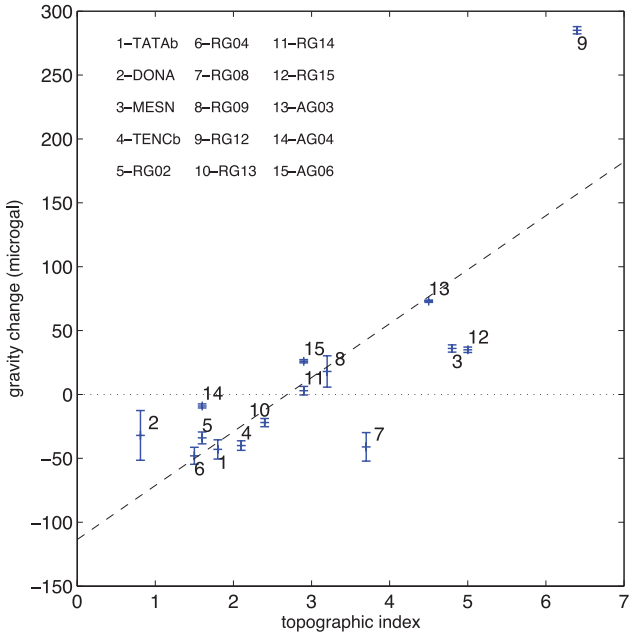

Figure 14. Comparison between the gravity changes observed between 2008 and 2010 in the Central Range and Western Foothills and the topographic index i_x at the same sites. The gravity changes are negative for most sites where $i_x < 2.5$ and conversely for positive gravity changes. At RG08 (#7) the relation fails: this site is indeed located near a large river-bed but a small landslide also occurred closer.

the topographic indices value at the gravity sites. The topographic index i_x is computed as

$$i_x = \ln\left(\frac{a}{\tan\beta}\right), \tag{5}$$

where a is the upslope area draining into each x location and β is the slope at x (Quinn *et al.* 1991). The computation is performed using Matlab functions provided by Schwanghart & Kuhn (2010) and a 90 m resolution Digital Elevation Model (DEM) of Taiwan. An area with high topographic indices (low slopes and high upslope draining area) can accumulate more materials than an area with low indices, which is rather likely to lose materials. The high or small topographic indices highlight areas where debris flow deposits or landslides could occur, respectively. Fig. 14 shows that gravity decreased where the topographic index is low and vice versa. Therefore, both Table 3, Figs 13 and 14 suggest that the large gravity changes in the Central Range and in the Western Foothills could be attributed to debris flow deposits and landslides. On the other hand, the gravity variations can be used to quantify these mass transfers as presented below.

4.2 Estimation of the thickness of debris flow deposits and landslides

4.2.1 Debris flow deposits

As a new application of gravity, here we show that we can determine the thickness of a debris flow deposit or of a landslide by

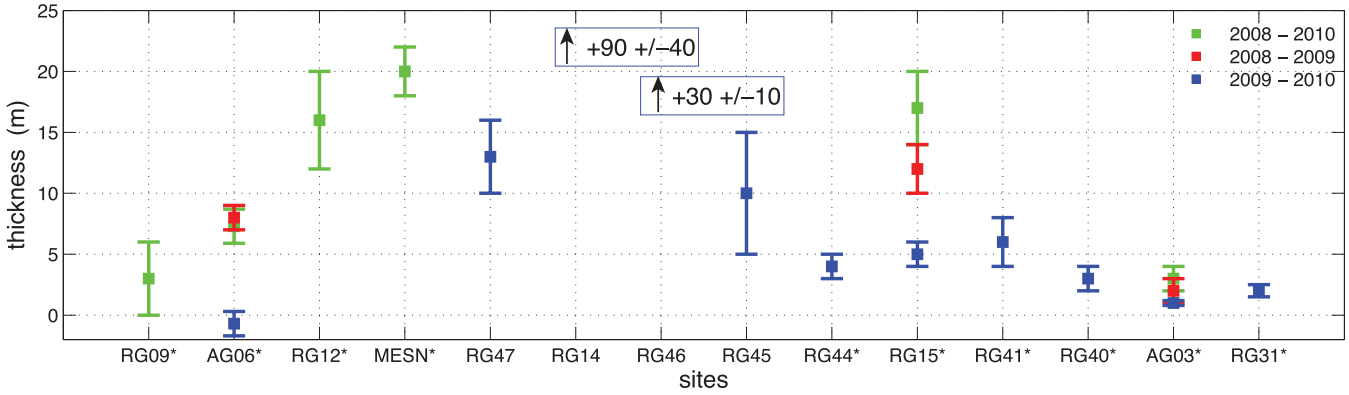

Figure 15. Thickness of debris flow deposits estimated using the gravity changes measured from 2008 to 2010. Depending on the survey repetition, the thickness can be computed using gravity changes observed between 2010 and 2008 (green), 2009 and 2008 (red) and 2010 and 2009 (blue). The names of the sites located nearby the river-beds are followed by an asterisk.

coupling the gravity change at a given site with its surrounding surface geometry obtained from satellite images and field observations (Fig. 13). The surface contours of the debris flow deposits were mapped near the gravity sites of the Central Range and the Western Foothills, using satellite images provided by Google Earth (http://www.google.com/earth). If a satellite image was acquired earlier than August 2009, the effect of typhoon Morakot, including the deposits, was not visible in the image and we used it to map river-beds only. Indeed, as debris flows were transported by rivers, we assumed that the debris flows geometries are constrained by the river-beds. We do not use the DEM, first because it does not contain information about Morakot deposits and, second, because its resolution (90 m) is too coarse to model river-beds. The surfaces were then divided into 15 m × 15 m rectangles and we added the thickness h as the third dimension (3-D). Thus each deposit was converted into 15 m × 15 m × h prisms. The thickness was finally estimated by 3-D forward gravity modelling, which only accounts for the Newtonian attraction of the prisms. As the deposits are made of materials removed from the Central Range and the Western Foothills, their average density is set to 2500 kg m^{-3} (Yen *et al.* 1998). Eventually, the estimated thickness depends on rock density, the gravity change and the location of the gravity site relative to the deposit (both laterally and vertically). The uncertainty of h was estimated from the uncertainty of the gravity change and from an arbitrary uncertainty of the vertical position of the site relative to the top of the deposit (usually ±10 m).

The estimated deposit thicknesses range from 1 to 20 m at sites located along the river-beds (sites with asterisks in Fig. 15). These estimates are consistent with the results from our field observations, especially at AG06, AG03, RG09 and RG12 (Fig. 13). The thicknesses estimated at the 4 sites located far from river-beds (RG47, RG14, RG46 anhd RG45) are arguable. These sites are in the most internal part of the Central Range and the gravity changes probably mix the attractions of several deposits or even landslides. Around these sites, we need more detailed information about all deposits and landslides to improve the mass balance and the interpretation of the gravity changes.

In the case of AG03, large gravity changes are observed since the first survey in 2006, so that Morakot typhoon (2009 August) cannot explain the entire time-series. As AG03 is located a few meters away from the large Peinan river-bed, we hypothesized that gravity changes were also influenced by the water level variations. These gravity changes are computed using

Table 4. Changes of the Peinan river level near AG03 pillar and comparison with expected and observed gravity variations, between 2006 and 2007.

Year	ΔH_w m)	Δg_{obs} (μGal)	Δg_{mod} (μGal)
2007	−1.8	-7 ± 4	−13
2008	−2.2	-15 ± 3	−16

Note: ΔH_w is the water level change in comparison with 2006. Δg_{mod} and Δg_{obs} are, respectively, the gravity changes modelled and observed, also in comparison with 2006.

records of the river level provided by the Water Resources Agency (http://gic.wra.gov.tw/gic/Water/Space/Main.aspx), only considering water masses (Table 4).

The gravity decrease observed from 2006 to 2008 is in agreement with the drop of the Peinan river. It supports the idea that gravity changes at AG03 basically record mass changes in the river. It is likely that this change also integrates the effects of rocks masses in addition to those of water. Indeed, even if there is no landslide, the large energy of the river during heavy rains may redistribute sediments of the bed. But we cannot separate the effects of rock and water in the gravity change.

It is interesting to note that large gravity increases are also observed between 2009 and 2010, in the Central Range (between RG31 and RG47). However, there was no strong typhoon (at least in comparison to Morakot) in Taiwan in 2010. A hypothesis is that materials eroded from the Central Range in August 2009 were not totally removed by the concomitant heavy rains. This is an example of transport-limited sediment discharge: rains became less powerful, thus had a lower transportation capacity (Hovius *et al.* 2000). Consequently, substantial sediment accumulations remained in the most internal areas of the Central Range. They were mobilized again by rains in summer 2010. Considering the gravity increases observed between 2009 and 2010, it is likely that our time-lapse gravimetry surveys have detected such a post-Morakot redistribution of the deposits over the Central Range.

4.2.2 Landslides

The same method is applied to study the effect of landslides on gravity changes. Here we chose to use the DEM because it provides the geometry of the area before the landslide occurred. The surface extension of the landslide is mapped on the DEM from field

observations (Fig. 13). Again, it is divided into 15 m × 15 m × h prisms, where h is the depth of the landslide detachment. We use the same mass density as for the debris flow deposits, that is, 2500 kg m^{-3}. DONA (Table 3) is the only site where there is enough information to perform this modelling, and here we found $h = 17 \pm 10$ m. Landslides have indeed occurred in the regions around RG02, RG03, RG04 and TATA because the roads were destroyed in several places here and RG03 was swept away. However, around RG02, RG04 and TATA, it was impossible to map these landslides as there is no scenic view and the satellite images at these places were taken before Morakot. We assume that the gravity changes at these sites are largely due to landslides, based on Fig. 14 and the inability of local land water and vertical ground motions to explain the large amplitude of these changes.

The quantification of the thickness of a landslide using gravity change is possible only if the landslide location and extension are known. On the contrary, the estimation of the thickness of a debris flow deposit is simpler because the corresponding location and geometry can be defined by river-beds.

4.3 Discussion on the use of gravimetry to quantify erosion processes

The gravity observations of these surface processes were not expected from the AGTO campaign, and demonstrate the potential application of temporal gravity change to erosion quantification. Typhoon Morakot, recognized as an anomalously strong event (e.g. Ge *et al.* 2010; Tsou *et al.* 2011), has enhanced this observation. A gravity network located in the vicinity of a river-bed can thus contribute to quantify sediment transfers. Some recommended improvements for such a network are as follows.

1. Increasing the number of gravity sites near the same deposit. This is practically possible because roads usually follow the river-beds. In addition, debris flows and other natural and man-made causes may destroy gravity sites (in our network, 6 sites have been swept away by landslides or debris flow). This situation will be improved by having redundant gravity sites in a given area to ensure a long, area-averaged record of gravity change from surviving sites.
2. Performing gravity surveys at least before (May) and after (October) the typhoon season, when largest mass transfers are likely to occur because of the rising energy of the rivers. The repetition of the surveys during the year will also improve the identification of the changes only due to local land water redistribution.
3. Monitoring the rivers level changes, in terms of water only. Again, this will allow a more reliable separation between the contributions from sediment and water masses to gravity changes.

Note that we did not measure the vertical gradient of gravity at the AG sites after the Morakot typhoon. At AG03, which is very close to a 3-m deposit, we compute that the gradient could decrease of 0.03 μGal cm^{-1}. This gradient error causes an error of 2 μGal in gravity when reducing the gravity value measured with the FG5 to the height of the CG-5 sensor. Although this error at AG03 is smaller than the CG-5 precision, larger errors could be reached for thicker deposits. Therefore, the vertical gravity gradients at AG sites near deposits or landslides should be re-measured.

5 CONCLUSIONS

In this study, we explained temporal gravity changes observed in southern Taiwan from 2006 to 2010 by vertical ground motions, local hydrology and massive mass transfers due to landslides and debris flow deposits. These effects were identified in the gravity time-series using GPS-derived heights, precipitation data and morphological changes of the land, respectively.

The hydrogravity model used in this study returned gravity changes that are consistent with the measurements at 7 of 10 AG sites (AG2a, AG2b, AG04, AG05, AG07, AG08 and AG09). However, the yearly frequency of the gravity surveys prevents from relying on the time constant of the charge of rain in the ground. A substantial improvement would be to make measurements during the raining seasons (spring and summer in Taiwan), at least, to better estimate this time constant. The gravity time-series in the Coastal Range and in the Western Foothills (AG2b, AG07 and the RG sites around) should be continued in order to study the effect of uplift on gravity change. In particular, a long record will allow an adequate determination of the $\Delta g/\Delta h$ ratio in an active subduction zone. In addition, a sustained campaign-mode gravity survey will provide valuable references for investigating the seismic cycle in connection to a major earthquake.

The large gravity changes measured in the Central Range and in the Western Foothills are related to the deposits of debris flows and landslides triggered by typhoon Morakot in August 2009. Using field observations, satellite images and 3-D gravity modelling, the gravity changes can be used to estimate the thickness of the deposit at 14 sites (ranging from 1 to 20 m in the river-beds) and the depth of the landslide detachment at one site (17 m). These results support that temporal gravimetry is a potentially new tool for monitoring and quantifying shallow mass transfers related to erosion processes. If a dense gravity network is deployed near a river-bed, for example, the rivers near AG06 and AG03, an in-depth understanding of the deposit variation of the river can be achieved.

ACKNOWLEDGMENTS

We thank editor Bert Vermeersen and two anonymous reviewers, which comments have greatly help to improve this manuscript. Maps were made with the generic mapping tools (GMT; Wessel & Smith 1991). We thank Jean-Paul Boy for computing the global hydrogravity effect computation (Fig. 7). We thank the Taiwanese institutes that maintain the permanent GPS and levelling benchmark networks, and the CWB for giving access to the GPS time-series. The CG-5 relative gravimeter used in this study was provided for by the Institut National des Sciences de l'Univers (INSU). The study is partially supported by the National Science Council of Taiwan (projects numbers: 98–2116-M-009–001, 99–2923-M-009–002, 100–2611-M-009–001), and the Ministry of the Interior of Taiwan (projects numbers: H950426, Y96014, C97013, DC98006, C99001).

REFERENCES

Altamimi, Z., Sillard, P. & Boucher, C., 2002. ITRF2000: A new release of the International Terrestrial Reference Frame for Earth science applications, *J. geophys. Res.,* **107**(B10), 2214, doi:10.1029/2001JB000561.

Ballu, V., Diament, M., Briole, P. & Ruegg, J.C., 2003. 1985–1999 gravity field variations across the Asal Rift: insights on vertical movements and mass transfer, *Earth planet. Sci. Lett.,* **208**(1–2), 41–49.

Beilin, J., 2006. Apport de la gravimétrie absolue à la réalisation de la composante gravimétrique du Réseau Géodésique Français, *Master thesis,* Inst. Geogr. Natl., Paris.

Bonvalot, S., Remy, D., Deplus, C., Diament, M. & Gabalda, G., 2008. Insights on the March 1998 eruption at Piton de la Fournaise volcano (La Reunion) from microgravity monitoring, *J. geophys. Res.,* **113**(B5), B05407, doi:10.1029/2007JB005084.

Bower, D. & Courtier, N., 1998. Precipitation effects on gravity measurements at the Canadian absolute gravity site, *Phys. Earth planet. Int.,* **106**(3–4), 353–369.

Boy, J. & Hinderer, J., 2006. Study of the seasonal gravity signal in superconducting gravimeter data, *J. Geodyn.,* **41**(1–3), 227–233.

Chen, C.S. & Chen, Y.L., 2003. The rainfall characteristics of Taiwan, *Mon. Wea. Rev.,* **131,** 1323–1341.

Cheng, J.D., Lin, L.L. & Lu, H.S., 2002. Influences of forests on water flows from headwater watersheds in Taiwan, *For. Ecol. Manage.,* **165,** 11–28.

Ching, K., Hsieh, M., Johnson, K., Chen, K., Rau, R. & Yang, M., 2011. Modern vertical deformation rates and mountain building in taiwan from precise leveling and continuous GPS observations, 2000–2008, *J. geophys. Res,* **116,** B08406, doi:10.1029/2011JB008242.

Creutzfeldt, B., Güntner, A., Wziontek, H. & Merz, B., 2010. Reducing local hydrology from high-precision gravity measurements: a lysimeter-based approach, *Geophys. J. Int.,* **183,** 178–187.

Crossley, D., Xu, S. & Van Dam, T., 1998. Comprehensive analysis of 2 years of SG data from Table Mountain, Colorado, in *Proceedings of the 13th Int. Symp. Earth Tides,* Brussels, pp. 659–668.

Crossley, D. *et al.*, 1999. Network of superconducting gravimeters benefits a number of disciplines, *EOS, Trans. Am. Geophys. Un.,* **80,** 121–126.

Dadson, S. *et al.*, 2003. Links between erosion, runoff variability and seismicity in the Taiwan orogen, *Nature,* **426**(6967), 648–651.

Dal Moro, G. & Zadro, M., 1998. Subsurface deformations induced by rainfall and atmospheric pressure: tilt/strain measurements in the ne-italy seismic area, *Earth planet. Sci. Lett.,* **164**(1–2), 193–203.

de Linage, C., Hinderer, J. & Rogister, Y., 2007. A search for the ratio between gravity variation and vertical displacement due to a surface load, *Geophys. J. Int.,* **171**(3), 986–994.

Debeglia, N. & Dupont, F., 2002. Some critical factors for engineering and environmental microgravity investigations, *J. appl. Geophys.,* **50**(4), 435–454.

Dehant, V., Defraigne, P. & Wahr, J.M., 1999. Tides for a convective Earth, *J. geophys. Res.,* **104,** 1035–1058.

Egbert, G.D. & Erofeeva, S.Y., 2002. Efficient inverse modeling of barotropic ocean tides, *J. Atmos. Oceanic Technol.,* **19**(2), 183–204.

Ek, M.B., Mitchell, K.E., Lin, Y., Rogers, E., Grunmann, P., Koren, V., Gayno, G. & Tarpley, J.D., 2003. Implementation of Noah land surface model advances in the National Centers for Environmental Prediction operational mesoscale Eta model, *J. geophys. Res.,* **108**(D22), 8851, doi:10.1029/2002JD003296.

Furuya, M., Okubo, S., Sun, W., Tanaka, Y., Oikawa, J., Watanabe, H. & Maekawa, T., 2003. Spatiotemporal gravity changes at Miyakejima Volcano, Japan: Caldera collapse, explosive eruptions and magma movement, *J. geophys. Res.,* **108**(B4), 2219, doi:10.1029/2002JB001989.

Ge, X., Li, T., Zhang, S. & Peng, M., 2010. What causes the extremely heavy rainfall in Taiwan during Typhoon Morakot (2009)?, *Atmos. Sci. Lett.,* **11**(1), 46–50.

Hofmann-Wellenhof, B. & Moritz, H., 2006. *Physical Geodesy,* Springer Verlag, Wien, 403, pp.

Hovius, N., Stark, C., Hao-Tsu, C. & Jiun-Chuan, L., 2000. Supply and removal of sediment in a landslide-dominated mountain belt: Central Range, Taiwan, *J. Geol.,* **108**(1), 73–89.

Hsu, S., 1998. Plan for a groundwater monitoring network in Taiwan, *Hydrogeol. J,* **6**(3), 405–415.

Huang, W., Johnson, K., Fukuda, J. & Yu, S., 2010. Insights into active tectonics of eastern Taiwan from analyses of geodetic and geologic data, *J. geophys. Res.,* **115**(B14), 03413.

Hugentobler, U., Schaer, S. & Fridez, 2001. Bernese GPS Software: Version 4.2, Astr. Inst., University of Berne.

Hwang, C., Wang, C.G. & Lee, L.H., 2002. Adjustment of relative gravity measurements using weighted and datum-free constraints, *Comput. Geosci.,* **28**(9), 1005–1015.

Hwang, C., Kao, R., Cheng, C.-C., Huang, J.F., Lee, C.W. & Sato, T., 2009. Results from parallel observations of superconducting and absolute gravimeters and GPS at the Hsinchu station of Global Geodynamics Project, Taiwan, *J. geophys. Res.,* **114**(B7), B07406, doi:10.1029/2008JB006195.

Hwang, W. & Wang, C., 1993. Sequential thrusting model for mountain building: constraints from geology and heat ow of Taiwan, *J. Geophys. Res.,* **98**(B6), 9963–9973.

Jacob, T., Bayer, R., Chery, J. & Le Moigne, N., 2010. Time-lapse microgravity surveys reveal water storage heterogeneity of a karst aquifer, *J. geophys. Res.,* **115**(B6), B06402, doi:10.1029/2009JB006616.

Kazama, T. & Okubo, S., 2009. Hydrological modeling of groundwater disturbances to observed gravity: Theory and application to asama volcano, central japan, *J. geophys. Res.,* **114**(B8), B08402.

Lambert, A. & Beaumont, C., 1977. Nano variations in gravity due to seasonal groundwater movements; implications for the gravitational detection of tectonic movements, *J. geophys. Res.,* **82**(2), 297–306, doi:10.1029/JB082i002p00297.

Letellier, T., Lyard, F. & Lefèvre, F., 2004. The new global tidal solution: Fes2004, in *Proceeding of the Ocean Surface Topography Science Team Meeting,* St. Petersburg, Florida, pp. 4–6.

Longuevergne, L., Boy, J.-P., Florsch, N., Viville, D., Ferhat, G., Ulrich, P., Luck, B. & Hinderer, J., 2009. Local and global hydrological contributions to gravity variations observed in Strasbourg, *J. Geodyn.,* **48**(3–5), 189 194.

Mäkinen, J., Engfeldt, A., Harsson, B.G., Ruotsalainen, H., Strykowski, G., Oja, T. & Wolf, D., 2005. The Fennoscandian land uplift gravity lines 1966–2003, in *Proceedings of the Gravity, Geoid and Space Missions, IAG Symposia,* Vol. 129, pp. 299–303, eds Jekeli, C., Bastos, L. & Fernandes, J., Springer Berlin Heidelberg.

Masson, F. *et al.*, 2008. Study of the Taiwanese Orogen from Absolute Gravity Data, in *Proceedings of the AGU Fall Meeting Abstracts,* San Francisco, Calif., pp. 2013.

Matsumoto, K., Sato, T., Takanezawa, T. & Ooe, M., 2001. Gotic2: A program for computation of oceanic tidal loading effect, *J. Geod. Soc. Jpn.,* **47**(1), 243–248.

Mazzotti, S., Lambert, A., Courtier, N., Nykolaishen, L. & Dragert, H., 2007. Crustal uplift and sea level rise in northern Cascadia from GPS, absolute gravity, and tide gauge data, *Geophys. Res. Lett.,* **34**(15), L15306.

Mazzotti, S., Lambert, A., Henton, J., James, T. & Courtier, N., 2011. Absolute gravity calibration of gps velocities and glacial isostatic adjustment in mid-continent North America, *Geophys. Res. Lett.,* **38**(24), L24311, doi:10.1029/2011GL049846.

Merriam, J.B., 1992. Atmospheric pressure and gravity, *Geophys. J. Int.,* **109**(3), 488–500.

Meurers, B., Van Camp, M. & Petermans, T., 2007. Correcting superconducting gravity time-series using rainfall modelling at the Vienna and Membach stations and application to Earth tide analysis, *J. Geod.,* **81**(11), 703–712.

Microg-LaCoste, 2006. FG5 Absolute Gravimeter User's Manual, Micro-g LaCoste, Inc., Lafayette, Colorado, EU, http://www.microglacoste.com/. Last accessed date: October 2012.

Microg-LaCoste, 2008. g8 Absolute Gravity Data Acquisition and Processing Software, Micro-g LaCoste, Inc., Lafayette, Colorado, EU, http://www.microglacoste.com/. Last accessed date: October 2012.

Mouyen, M. *et al.*, 2009. Expected temporal absolute gravity change across the Taiwanese Orogen, a modeling approach, *J. Geodyn.,* **48,** 284–291.

Morishita, Y. & Heki, K., 2008. Characteristic precipitation patterns of El Niño/La Niña in time variable gravity fields by GRACE, *Earth planet. Sci. Lett.,* **272**(3–4), doi:10.1016/j.epsl.2008.06.003.

Naujoks, M., Weise, A., Kroner, C. & Jahr, T., 2008. Detection of small hydrological variations in gravity by repeated observations with relative gravimeters, *J. Geod.,* **82**(9), 543–553.

Niebauer, T.M., Sasagawa, G.S., Faller, J.E., Hilt, R. & Klopping, F., 1995. A new generation of absolute gravimeters, *Metrologia,* **32,** 159–180.

Peyret, M., Dominguez, S., Cattin, R., Champenois, J., Leroy, M. & Zajac, A., 2011. Present-day interseismic surface deformation along the Longitudinal Valley, eastern Taiwan, from a PS-InSAR analysis of the ERS satellite archives, *J. geophys. Res.,* **116**(B3), B03402, doi:10.1029/2010JB007898.

Pfeffer, J. *et al.*, 2010. Local and global hydrological contributions to time-variable gravity in Southwest Niger, *Geophys. J. Int.,* **184**(2), 661–672.

Quinn, P., Beven, K., Chevallier, P. & Planchon, O., 1991. The prediction of hillslope flow paths for distributed hydrological modelling using digital terrain models, *Hydrol. Process.,* **5**(1), 59–79.

Rodell, M. *et al.*, 2004. The global land data assimilation system, *Bull. Am. Meteorol. Soc.,* **85**(3), 381–394.

Scherneck, H., 1991. A parametrized solid Earth tide model and ocean tide loading effects for global geodetic baseline measurements, *Geophys. J. Int.,* **106**(3), 677–694.

Schwanghart, W. & Kuhn, N., 2010. TopoToolbox: A set of Matlab functions for topographic analysis, *Environ. Modell. Software,* **25**(6), 770–781.

Scintrex, 2006. CG-5 Scintrex Autograv System, Operation Manual, Sintrex Limited, Concord, Ontario, Canada, http://www.scintrex.com/. Last accessed date: October 2012.

Shin, T., Kuo, K., Leu, P., Tsai, C. & Jiang, J., 2011. Continuous cwb gps array in taiwan and applications to monitoring seismic activity, *Terr. Atmos. Oceanic Sci.,* **22**(5), 521–533.

Shum, C.K. *et al.*, 2011. Inter-annual water storage changes in Asia from GRACE data, in *Climate Change and Food Security in South Asia,* eds Lal, R., Sivakumar, M., Faiz, S.M.A., Mustafizur Rahman, A.H.M. & Islam, K.R. *et al.*, Springer-Verlag, Dordrecht, doi:10.1007/978-90-481-9516-9_6.

Shyu, J., Sieh, K., Chen, Y. & Liu, C., 2005. Neotectonic architecture of Taiwan and its implications for future large earthquakes, *J. geophys. Res.,* **110**(B8), B08402, doi:10.1029/2004JB003251.

Simoes, M., Beyssac, O. & Chen, Y.G., 2012. Late Cenozoic metamorphism and mountain building in Taiwan: A review, *J. Asian Earth Sci.,* **46,** doi:10.1016/j.jseaes.2011.11.009.

Torge, W., 1989. *Gravimetry,* Walter de Gruyter, Berlin, 465 pp.

Tsai, F., Hwang, J., Chen, L. & Lin, T., 2010. Post-disaster assessment of landslides in southern Taiwan after 2009 typhoon Morakot using remote sensing and spatial analysis, *Nat. Hazards Earth Syst. Sci.,* **10,** 2179–2190.

Tsou, C., Feng, Z. & Chigira, M., 2011. Catastrophic landslide induced by Typhoon Morakot, Shiaolin, Taiwan, *Geomorphology,* doi:10.1016/j.geomorph.2010.12.013.

Van Camp, M. & Vauterin, P., 2005. Tsoft: graphical and interactive software for the analysis of time series and Earth tides, *Comput. Geosci.,* **31**(5), 631–640.

Van Camp, M., Williams, S.D.P. & Francis, O., 2005. Uncertainty of absolute gravity measurements, *J. geophys. Res,* **110,** B05406, doi:10.1029/2004JB003497.

Van Camp, M., Métivier, L., de Viron, O., Meurers, B. & Williams, S.D.P., 2010. Characterizing long-time scale hydrological effects on gravity for improved distinction of tectonic signals, *J. geophys. Res.,* **115**(B7), B07407, doi:10.1029/2009JB006615.

Van Camp, M., de Viron, O., Scherneck, H., Hinzen, K., Williams, S., Lecocq, T., Quinif, Y. & Camelbeeck, T., 2011. Repeated absolute gravity measurements for monitoring slow intraplate vertical deformation in western Europe, *J. geophys. Res.,* **116**(B8), B08402, doi:10.1029/2010JB008174.

Virtanen, H., 2001. Hydrological studies at the gravity station Metsahovi, Finland, *J. Geodet. Soc. Jpn.,* **47**(1), 328–333.

Wenzel, G., 2002. Etgtab version 3.0. Earth tide prediction program, Tech. Rep., Retrieved 2002 April 11 fromhttp://www1.gik.uni-karlsruhe.de/wenzel10.1093/gji/ggs019.html.

Wessel, P. & Smith, W.H.F., 1991. Free software helps map and display data, *EOS, Trans. Am. geophys. Un.,* **72,** 441.

Williams, S.D.P., 2008. CATS: GPS coordinate time series analysis software, *GPS Sol.,* **12**(2), 147–153.

Xie, P. & Arkin, P.A., 1997. Global precipitation: a 17-year monthly analysis based on gauge observations, satellite estimates, and numerical model outputs, *Bull. Am. Meteorol. Soc.,* **78**(11), 2539–2558.

Yamato, P., Mouthereau, F. & Burov, E., 2009. Taiwan mountain building: insights from 2-D thermomechanical modelling of a rheologically stratified lithosphere, *Geophys. J. Int.,* **176**(1), 307–326.

Yen, H.Y., Yeh, Y.H. & Wu, F.T., 1998. Two-dimensional crustal structures of Taiwan from gravity data, *Tectonics,* **17,** 104–111.

Yu, S.B., Chen, H.Y. & Kuo, L.C., 1997. Velocity field of GPS stations in the Taiwan area, *Tectonophysics,* **274**(1–3), 41–59.

APPENDIX A

The following graphs are the GPS and rainfall time-series measured at site located near each of the AG site (see Fig. 8 for their locations). The title above the subplots is the name of the AG site. Below, the vertical component of the closest GPS site, used for ground motion correction, is given. The name of the GPS station is on the *y*-axis. The second graph below is the precipitation record, used for the hydrogravity model. Thus, one AG site is associated to two subplots. The vertical dashed lines give the time of the AG measurement for each site. The red line in the precipitation graphs is the number of missing hourly records per day (same axis as bars). Indeed we compute daily rains from hourly records. Thus it spans values between 0 and 24 (the limit at 24 is the short dashed red line). The large step (30 cm) in the GPS time-series at MOTN (AG04) is considered as an artefact as nothing near the antenna can confirm this uplift (moreover the horizontal components show no particular change at the same time). The step is cancelled by linearly extrapolating the initial GPS trend up to the time of the last gravity measurement. The GPS time-series recorded by CK01 stopped before the last gravity measurement at AG08. As for MOTN the GPS time-series is linearly extrapolated up to the time of the last gravity measurement.

APPENDIX B

Fit of the hydrogravity model (blue line with τ_1 and τ_2 parameters, see Section 3.1) to the RG time-series corrected from vertical ground motions (red squares) concurrently measured by permanent GPS, or not (black dots). The values below each plot are the rms misfits, in μGal, for both cases (same colour code). Sites are located on the following tectonic units: S104 to RG39 = Coastal Range; TTUNb to LONTb = Longitudinal Valley; TMLM to MESN = Central Range; RG12 to TATAb = Western Foothills; ICHU to SJPU = Coastal Plain.

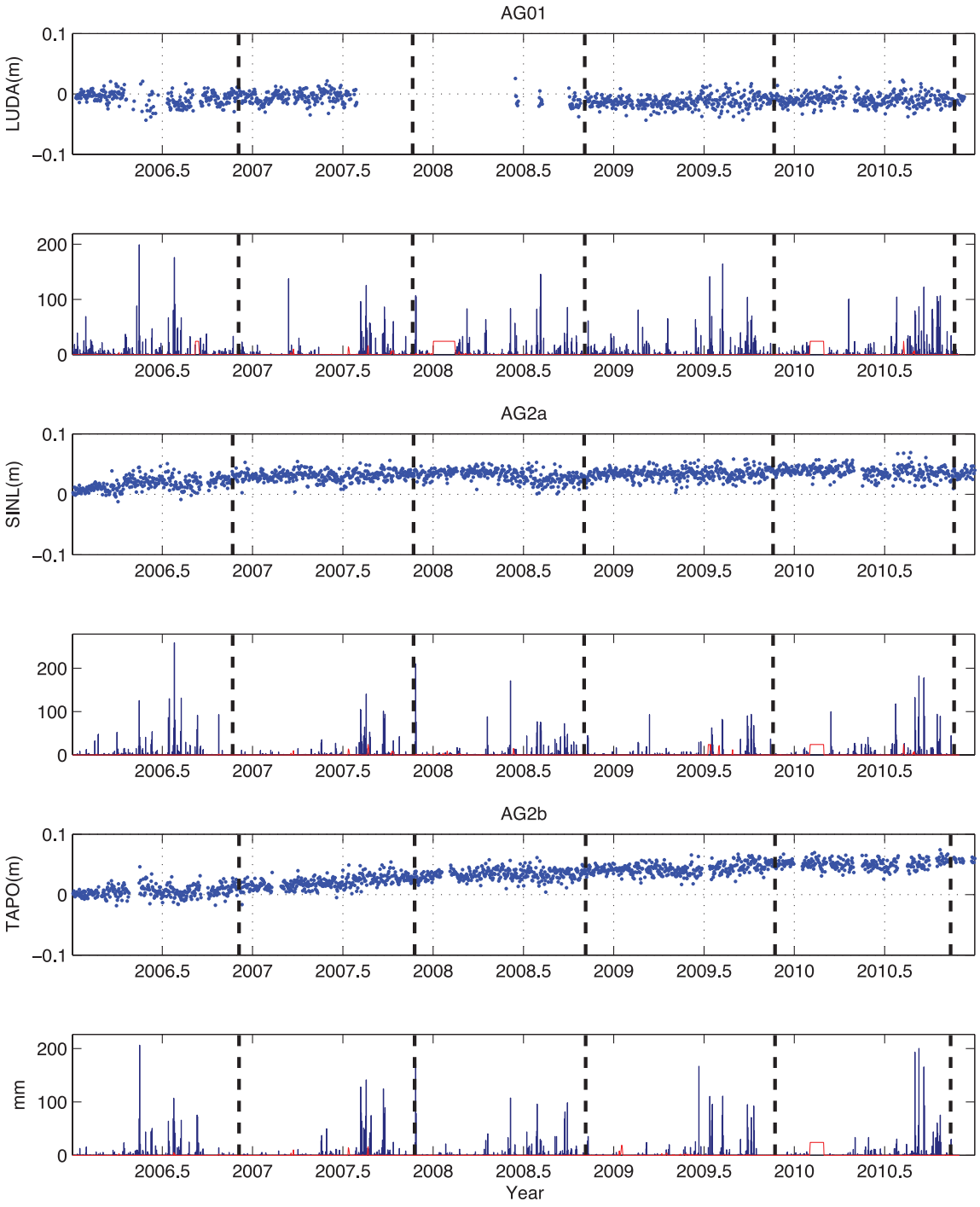

Figure A1.

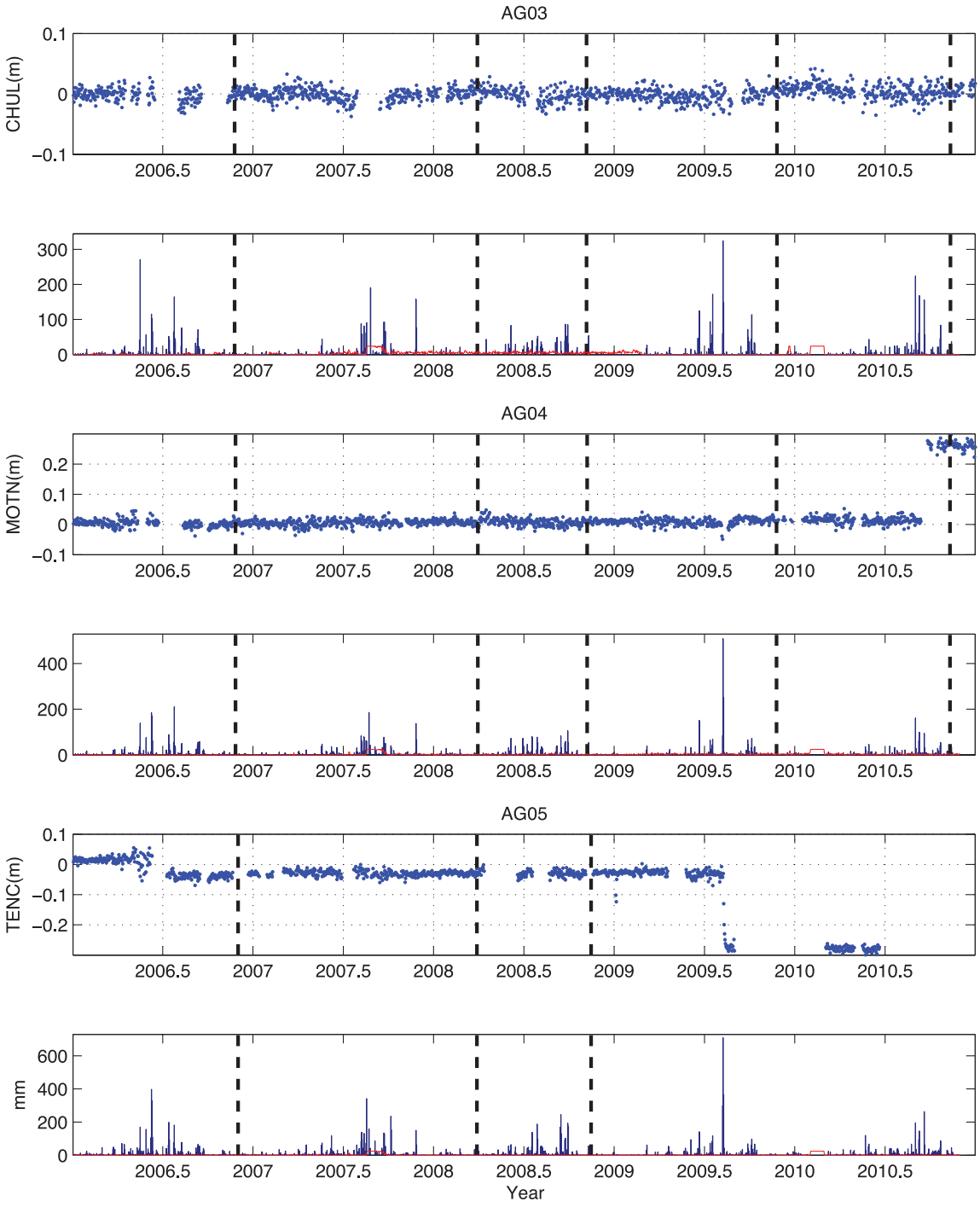

Figure A1. (*Continued.*)

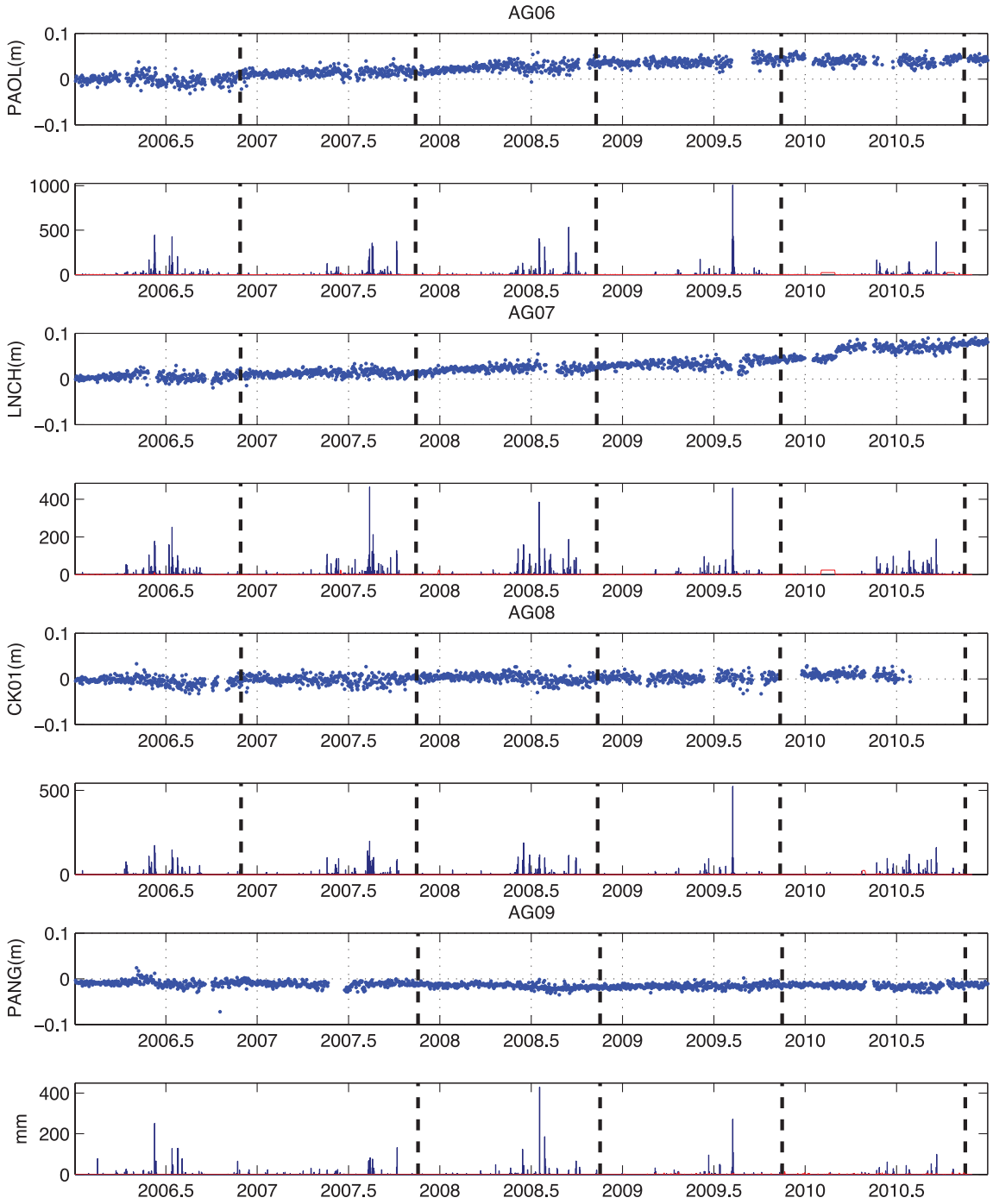

Figure A1. (*Continued.*)

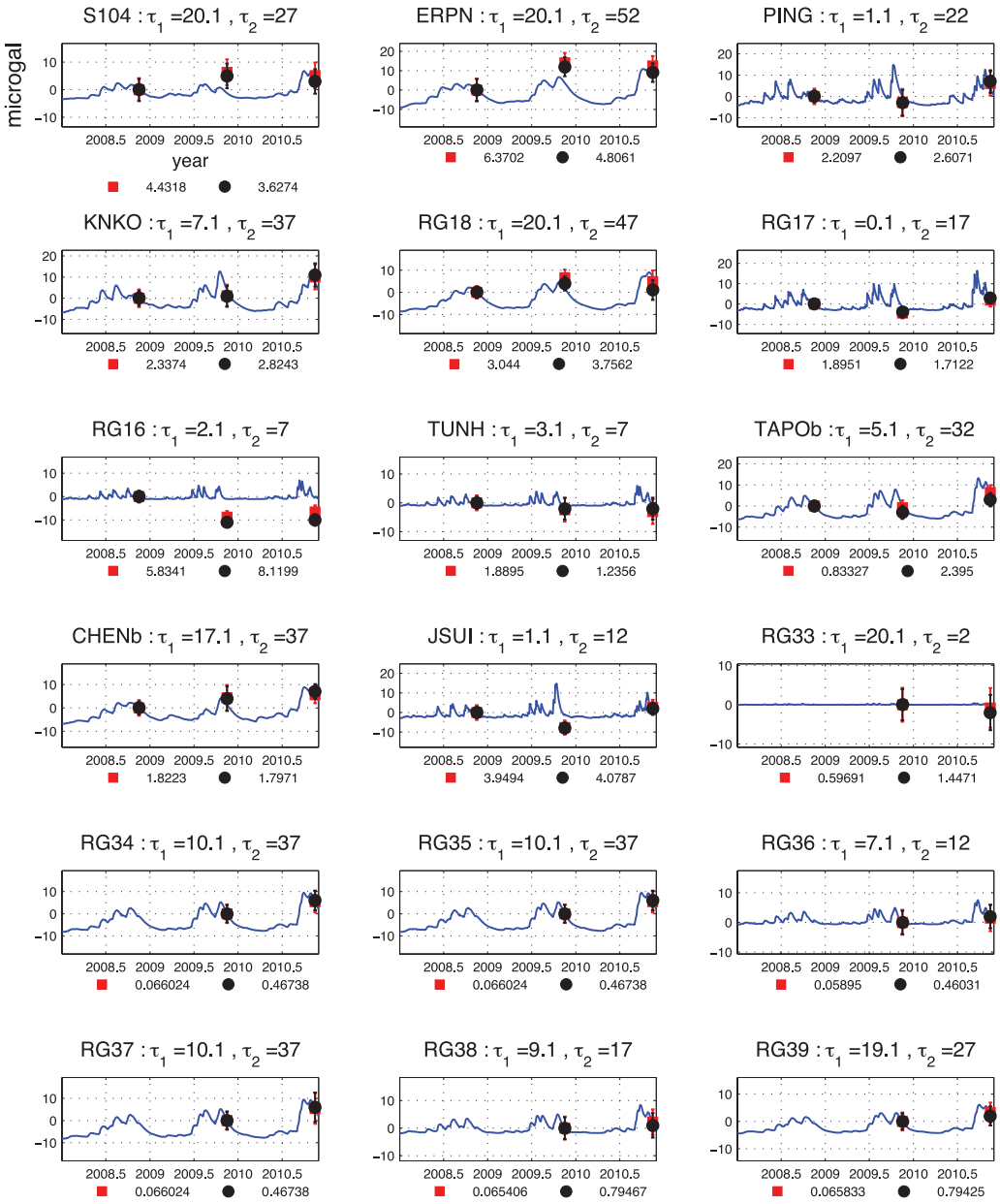

Figure B1.

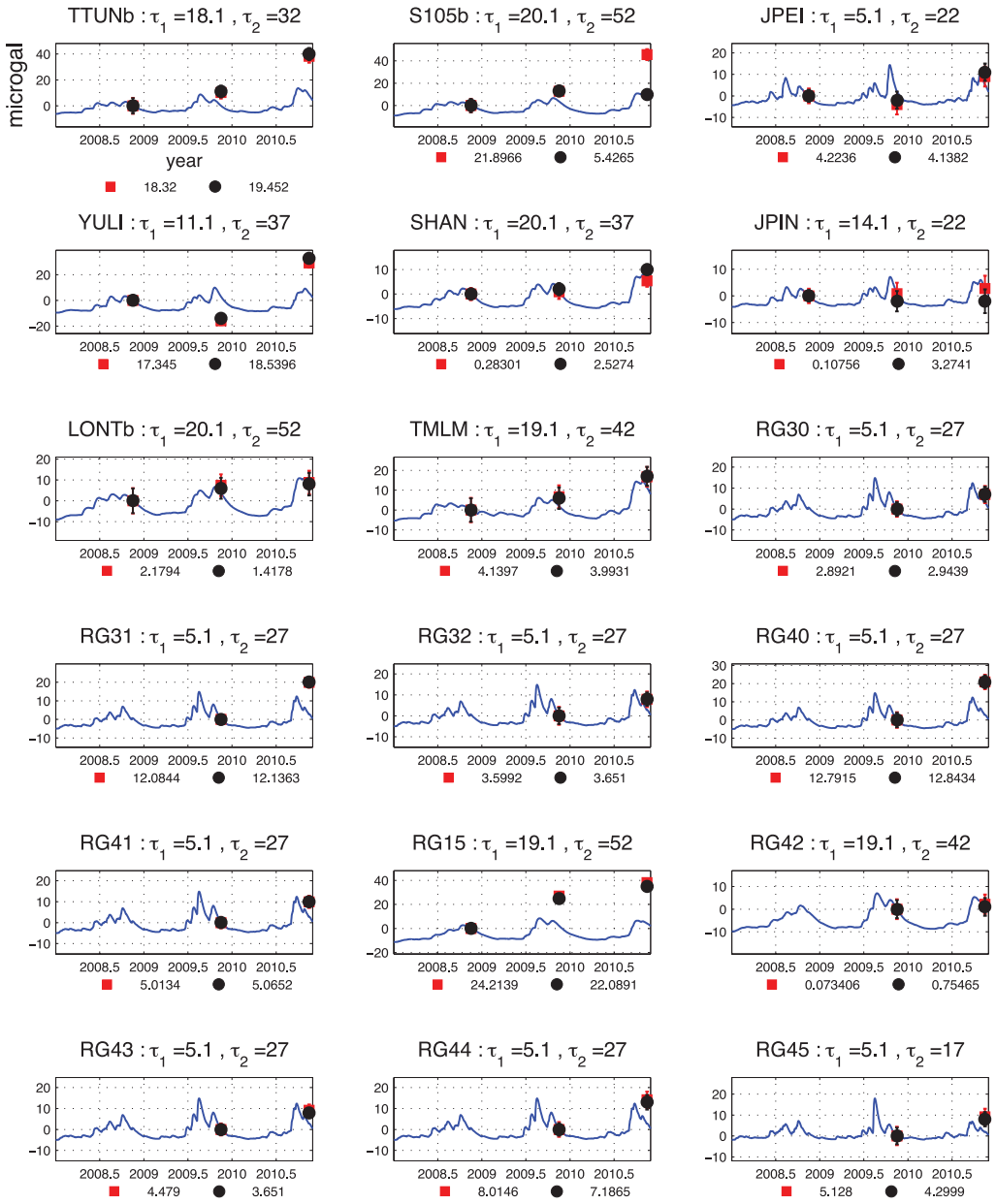

Figure B1. (*Continued.*)

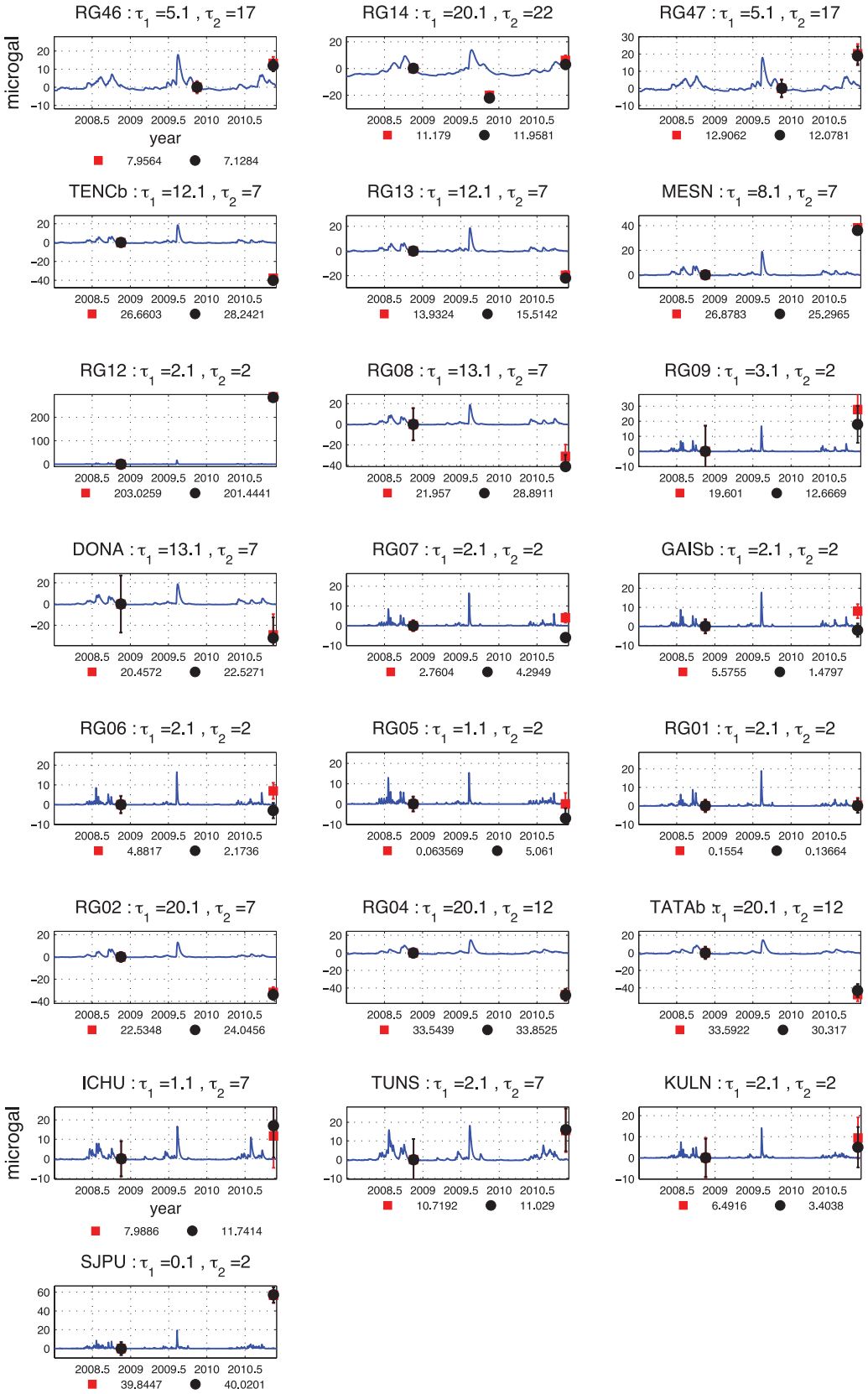

Figure B1. (*Continued.*)